

NAVAL POSTGRADUATE SCHOOL

Monterey, California

AD-A247 151



THESIS

SIMULATION OF ATMOSPHERIC FRONTOGENESIS WITH A
SEMI-LAGRANGIAN NUMERICAL MODEL

by

Ricardo Carvalho de Almeida

September 1991

Thesis Advisor:

Roger Terry Williams

Approved for public release; distribution is unlimited

92 3 06 026

92-06036



REPORT DOCUMENTATION PAGE			
1a REPORT SECURITY CLASSIFICATION Unclassified		1b RESTRICTIVE MARKINGS	
2a SECURITY CLASSIFICATION AUTHORITY		3 DISTRIBUTION/AVAILABILITY OF REPORT Approved for public release; distribution is unlimited.	
2b DECLASSIFICATION/DOWNGRADING SCHEDULE			
4 PERFORMING ORGANIZATION REPORT NUMBER(S)		5 MONITORING ORGANIZATION REPORT NUMBER(S)	
6a NAME OF PERFORMING ORGANIZATION Naval Postgraduate School	6b OFFICE SYMBOL (If applicable) 55	7a NAME OF MONITORING ORGANIZATION Naval Postgraduate School	
6c ADDRESS (City, State, and ZIP Code) Monterey, CA 93943-5000		7b ADDRESS (City, State, and ZIP Code) Monterey, CA 93943-5000	
8a NAME OF FUNDING/SPONSORING ORGANIZATION	8b OFFICE SYMBOL (If applicable)	9. PROCUREMENT INSTRUMENT IDENTIFICATION NUMBER	
8c ADDRESS (City, State, and ZIP Code)		10 SOURCE OF FUNDING NUMBERS	
		Program Element No	Project No
		Task No	Work Unit Accession Number
11 TITLE (Include Security Classification) SIMULATION OF ATMOSPHERIC FRONTOGENESIS WITH A SEMI-LAGRANGIAN NUMERICAL MODEL			
12 PERSONAL AUTHOR(S) Ricardo Carvalho de Almeida			
13a TYPE OF REPORT Master's Thesis	13b TIME COVERED From To	14 DATE OF REPORT (year, month, day) September 1991	15 PAGE COUNT 70
16 SUPPLEMENTARY NOTATION The views expressed in this thesis are those of the author and do not reflect the official policy or position of the Department of Defense or the U.S. Government.			
17. COSATI CODES		18. SUBJECT TERMS (continue on reverse if necessary and identify by block number)	
FIELD	GROUP	SUBGROUP	
		Meteorology, Numerical Weather Prediction, Semi-Lagrangian, Frontogenesis	
19 ABSTRACT (continue on reverse if necessary and identify by block number)			
<p>In this study a numerical model based on the hydrostatic Boussinesq equations is used to simulate atmospheric frontogenesis driven by an irrotational non-divergent deformation wind field. The equations are numerically integrated by using the semi-Lagrangian technique associated with two different time schemes: explicit and semi-implicit. Both schemes produce realistic fronts after approximately 40 hours of model integration. The semi-Lagrangian semi-implicit scheme is more successful in handling the sharp gradients associated with the front. Also, the semi-Lagrangian semi-implicit equations are integrated with time steps as long as 3600 sec. producing solutions with relatively small errors. This indicates that this numerical scheme is appropriate for use in mesoscale regional models.</p>			
20. DISTRIBUTION/AVAILABILITY OF ABSTRACT		21. ABSTRACT SECURITY CLASSIFICATION	
<input checked="" type="checkbox"/> UNCLASSIFIED/UNLIMITED <input type="checkbox"/> SAME AS REPORT <input type="checkbox"/> DTIC USERS		Unclassified	
22a NAME OF RESPONSIBLE INDIVIDUAL Roger T. Williams		22b TELEPHONE (Include Area code) (408) 646-2296	22c OFFICE SYMBOL MR/WU

Approved for public release; distribution is unlimited.

Simulation of Atmospheric Frontogenesis with a Semi-Lagrangian Numerical Model

by

Ricardo Carvalho de Almeida
Lieutenant Commander, Brazilian Navy
B.S., Brazilian Naval Academy

Submitted in partial fulfillment
of the requirements for the degree of


MASTER OF SCIENCE IN METEOROLOGY AND PHYSICAL OCEANOGRAPHY

from the

NAVAL POSTGRADUATE SCHOOL

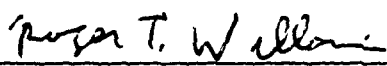
September 1991

Author:

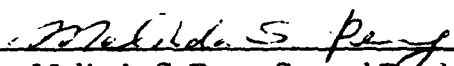


Ricardo C. Almeida

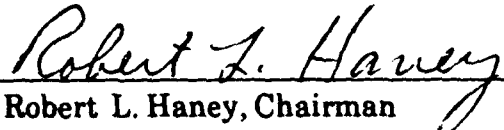
Approved by:



Roger T. Williams, Thesis Advisor



Melinda S. Peng, Second Reader



Robert L. Haney, Chairman
Department of Meteorology

ABSTRACT

In this study a numerical model based on the hydrostatic Boussinesq equations is used to simulate atmospheric frontogenesis driven by an irrotational non-divergent deformation wind field. The equations are numerically integrated by using the semi-Lagrangian technique associated with two different time schemes: explicit and semi-implicit. Both schemes produce realistic fronts after approximately 40 hours of model integration. The semi-Lagrangian semi-implicit scheme is more successful in handling the sharp gradients associated with the front. Also, the semi-Lagrangian semi-implicit equations are integrated with time steps as long as 3600 sec. producing solutions with relatively small errors. This indicates that this numerical scheme is appropriate for use in mesoscale regional models.

Accession For	
NTIS GRA&I	<input checked="" type="checkbox"/>
DTIC TAB	<input type="checkbox"/>
Unannounced	<input type="checkbox"/>
Justification	
By _____	
Distribution/_____	
Availability Codes	
Dist	Avail and/or Special
A-1	

TABLE OF CONTENTS

I. INTRODUCTION	1
II. THE SEMI-LAGRANGIAN SCHEME	3
III. BASIC EQUATIONS	6
IV. NUMERICAL SOLUTION	17
A. INITIAL CONDITIONS	17
B. THE SPATIAL GRID	20
C. FORMULATION OF THE MODELS	20
1. Semi-Lagrangian Explicit Scheme	20
2. Semi-Lagrangian Semi-Implicit Scheme	22
V. EXPERIMENTS AND RESULTS	31
A. PARAMETERS USED IN THE EXPERIMENTS	31
B. DESCRIPTION OF THE EXPERIMENTS	34
VI. SUMMARY AND CONCLUSIONS	58
LIST OF REFERENCES	60

INITIAL DISTRIBUTION LIST 62

I. INTRODUCTION

The development of fast computers has been of great importance for the atmospheric sciences. With them, scientists have been able to obtain a better understanding of the physical processes in the atmosphere and operational weather services have produced more accurate forecasts. But as pointed out by Robert (1981), scientists can also give their contribution by developing numerical algorithms that are computationally less expensive and at the same time accurate. This interaction between science and technology will allow the computational effort to be used in numerical models that will have higher resolution and that will be more accurate, as well, since more realistic and complex physical processes would be represented in these models.

One of the atmospheric processes that has been under active study is the formation of fronts. In a study of non-geostrophic frontogenesis Williams(1972) reproduced numerically a realistic front, demonstrating the importance of nonlinear effects in this dynamical process. Since frontogenesis is a phenomenon that is characterized by the development of sharp gradients of the physical parameters it would be interesting to develop a numerical model based on techniques that can handle adequately the scale collapse problem. Kuo and Williams (1990) studied the use of different numerical techniques in the solution of a simple scale collapse problem. They concluded that the semi-Lagrangian method, developed by Sawyer (1963), would be adequate for use in numerical models where strong gradients were present.

The semi-Lagrangian technique has been used mostly in synoptic scale numerical models. Robert (1981) used this technique with the semi-implicit scheme (Robert et al.,

1972) in a primitive equation model and obtained perfectly stable solutions using time steps 25 times larger than those that would be allowed by the Courant-Friedrichs-Lewy (CFL) stability criterion. Pudykiewicz and Staniforth (1984) examined the use of the scheme in several different conditions and concluded that besides its good stability properties, it is also accurate and flexible.

The objective of the present study is to perform experiments using the semi-Lagrangian technique in a frontogenesis model and verify its suitability for use in the representation of atmospheric processes where sharp gradients are present.

The semi-Lagrangian technique is introduced in the next chapter. The basic model equations are developed in chapter III. The numerical procedure employed for solving the equations is presented in chapter IV. In chapter V the experiments and results are discussed, followed by the summary and conclusions in chapter VI.

II. THE SEMI-LAGRANGIAN SCHEME

This model uses a semi-Lagrangian algorithm similar to the one described by Robert (1981).

The three time level semi-Lagrangian technique consists of evaluating the total derivative of a general dependent variable $Q(\vec{r}(t), t)$ following the trajectory of the fluid particle, using the approximation

$$\frac{dQ}{dt} = \frac{Q(\vec{r}(t+\Delta t), t+\Delta t) - Q(\vec{r}(t-\Delta t), t-\Delta t)}{2\Delta t}, \quad (2.1)$$

where $\vec{r}(t)$ represents the position vector of the fluid particle at time t . For sake of simplicity, constrain the problem to two dimensions, y and z . In this case the position vector will be

$$\vec{r}(t) = y(t)\vec{j} + z(t)\vec{k}. \quad (2.2)$$

The location of the particle at the forecast time $(t + \Delta t)$ is chosen to be coincident with a grid point. Let the displacements of the particle along the y and z directions

during one time step be represented by a and b , respectively. If the grid point position is represented by

$$\vec{r}(t + \Delta t) = (y_j, z_k) \quad (2.3)$$

the approximation (2.1) can be written as

$$\frac{dQ}{dt} = \frac{Q(y_j, z_k, t + \Delta t) - Q(y_j - 2a, z_k - 2b, t - \Delta t)}{2\Delta t} \quad (2.4)$$

The displacements a and b can be calculated iteratively using

$$a^{n+1} = \Delta t \cdot v(y_j - a^n, z_k - b^n, t), \quad (2.5a)$$

$$b^{n+1} = \Delta t \cdot w(y_j - a^n, z_k - b^n, t), \quad (2.5b)$$

where the superscript n represents the n^{th} iteration and v and w represent the horizontal and vertical velocities, respectively. The initial estimates of a and b in the iterative process are defined by

$$a^0 = \Delta t \cdot v(y_j, z_k, t), \quad (2.5c)$$

$$b^0 = \Delta t \cdot w(y_j, z_k, t) \quad (2.5d)$$

In Pudykiewicz and Staniforth (1984) it can be found that the necessary condition for convergence of the iterative procedure described in (2.5) is

$$\Delta t \cdot \max \left(\left| \frac{\partial v}{\partial y} \right|, \left| \frac{\partial v}{\partial z} \right|, \left| \frac{\partial w}{\partial y} \right|, \left| \frac{\partial w}{\partial z} \right| \right) < 1. \quad (2.6)$$

Furthermore, Kuo and Williams (1990) point out that no more than three iterations are necessary for convergence to be attained. Robert (1981) compared the use of two and four iterations in his primitive equation model and the results obtained were quite similar.

In order to determine the values of the variable Q at time $t - \Delta t$ it is necessary to use an interpolation scheme. In this model, bicubic spline interpolations (de Boor, 1962) were used with the explicit formulations of the semi-Lagrangian scheme, using the algorithm described by Marchuck (1982). In the semi-implicit formulation only one-dimensional cubic splines in the y direction are necessary to solve the problem; as will be shown in IV.C.2.

III. BASIC EQUATIONS

This model uses the hydrostatic Boussinesq equations, which assume incompressibility of the atmosphere. Friction and heating are neglected. It is also assumed that the atmosphere is bounded above by a rigid lid. Periodic boundary conditions are used in the horizontal.

The Boussinesq equations can be written as

$$\frac{du}{dt} = -\frac{\partial\phi}{\partial x} + fv, \quad (3.1)$$

$$\frac{dv}{dt} = -\frac{\partial\phi}{\partial y} - fu, \quad (3.2)$$

$$\frac{\partial u}{\partial x} + \frac{\partial v}{\partial y} + \frac{\partial w}{\partial z} = 0, \quad (3.3)$$

$$\frac{d\theta}{dt} = 0, \quad (3.4)$$

$$\frac{\partial \varphi}{\partial z} = \frac{g\theta}{\theta_0}, \quad (3.5)$$

where

$$\kappa = \frac{R}{C_p}, \quad (3.6)$$

$$\theta = T \left(\frac{p}{p_0} \right)^\kappa - \theta_0, \quad (3.7)$$

$$\varphi = C_p \theta_0 \left(\frac{p}{p_0} \right)^\kappa + gz. \quad (3.8)$$

This model assumes that the Coriolis parameter f is constant, and that the bottom topography is flat. The variations in the x direction, along the front, are neglected, except for the φ field and the basic deformation field.

With the assumptions above, equation (3.3) reduces to

$$\frac{\partial v}{\partial y} + \frac{\partial w}{\partial z} = 0 \quad (3.9)$$

for departures from the deformation wind field.

With the use of a rigid lid assumption the pressure is not known at any level, and this will require some manipulation of the equations.

Integrate the hydrostatic equation (3.5) from $z = 0$ to an arbitrary level z and obtain

$$\varphi = \int_0^z \frac{g\theta}{\theta_0} dz + C. \quad (3.10)$$

The constant of integration, C , can be determined by taking the vertical average of equation (3.10) and subtracting from equation (3.10) which gives

$$\varphi = \frac{g}{\theta_0} \int_0^z \theta dz - \left\langle \frac{g}{\theta_0} \int_0^z \theta dz \right\rangle + \langle \varphi \rangle, \quad (3.11)$$

where $\langle \rangle$ denotes the vertical average operator

$$\langle F \rangle = \frac{1}{H} \int_0^H F dz. \quad (3.12)$$

The constant of integration has been eliminated, but now an expression for $\langle \varphi \rangle$ must be found.

Apply the vertical average operator to the continuity equation (3.9) and use the vertical boundary conditions

$$w = 0 \quad \text{at} \quad z = 0 \quad (3.13a)$$

and

$$w = 0 \quad \text{at} \quad z = H \quad (3.13b)$$

which yields

$$\frac{\partial \langle v \rangle}{\partial y} = 0. \quad (3.14)$$

Next, expand the total derivative in equation (3.2), multiply (3.9) by v and add to (3.2) to obtain

$$\frac{\partial v}{\partial t} + \frac{\partial vv}{\partial y} + \frac{\partial wv}{\partial z} = -\frac{\partial \phi}{\partial y} - fu. \quad (3.15)$$

Take the vertical average of (3.15), using the vertical boundary conditions (3.13), which gives

$$\frac{\partial \langle v \rangle}{\partial t} + \frac{\partial \langle vv \rangle}{\partial y} = -\frac{\partial \langle \phi \rangle}{\partial y} - f \langle u \rangle. \quad (3.16)$$

Differentiating (3.16) with respect to y and using equation (3.14) yields

$$\frac{\partial^2 \langle \varphi \rangle}{\partial y^2} = - \frac{\partial^2 \langle vv \rangle}{\partial y^2} - f \frac{\partial \langle u \rangle}{\partial y}. \quad (3.17)$$

With appropriate boundary conditions, a solution for $\langle \varphi \rangle$ can be found.

In order to solve equation (3.1), an expression for $\frac{\partial \varphi}{\partial x}$ must be obtained. Differentiate (3.11) with respect to x and use the assumption that θ is not a function of x which gives

$$\frac{\partial \varphi}{\partial x} = \frac{\partial \langle \varphi \rangle}{\partial x}. \quad (3.18)$$

An expression for $\frac{\partial \langle \varphi \rangle}{\partial x}$ must be obtained. Take the domain average of (3.2)

$$\left\langle \frac{dv}{dt} \right\rangle = \left\langle - \frac{\partial \varphi}{\partial y} \right\rangle - \langle fu \rangle, \quad (3.19)$$

where $\{ () \}$ denotes the horizontal average operator

$$\{F\} = \frac{1}{L} \int_{-\frac{L}{2}}^{\frac{L}{2}} F dy. \quad (3.20)$$

Expand the first term of (3.19) and use the vertical boundary conditions (3.13) which yields

$$\left\langle \frac{dv}{dt} \right\rangle = \frac{\partial \langle v \rangle}{\partial t} = \frac{\partial \langle v \rangle}{\partial t}. \quad (3.21)$$

Using periodic boundary conditions in the y direction, it can be shown that the second term in (3.19) is zero. With the assumption of constant f , and using (3.21), equation (3.19) becomes

$$\frac{\partial \langle v \rangle}{\partial t} = -f \langle u \rangle. \quad (3.22)$$

Likewise, take the domain average of (3.1) and use the vertical and horizontal boundary conditions which yields

$$\frac{\partial \langle u \rangle}{\partial t} = -\frac{\partial \langle \varphi \rangle}{\partial x} + f \langle v \rangle. \quad (3.23)$$

Equations (3.22) and (3.23) show that if $\langle u \rangle$ is set initially equal to zero, $\langle v \rangle$ will remain constant in time and so will $\frac{\partial \langle \varphi \rangle}{\partial x}$. Furthermore, if $\langle v \rangle$ is also set to zero initially, $\frac{\partial \langle \varphi \rangle}{\partial x}$ will be identically zero for all time.

In this study it will be further assumed that $\frac{\partial \langle \varphi \rangle}{\partial x}$ is constant in the cross frontal direction (y), which allows to write

$$\frac{\partial \{ \langle \varphi \rangle \}}{\partial x} = \frac{\partial \langle \varphi \rangle}{\partial x} \quad (3.24)$$

With the assumptions above the following relation is obtained

$$\frac{\partial \varphi}{\partial x} - \frac{\partial \langle \varphi \rangle}{\partial x} = 0, \quad (3.25)$$

for initial conditions

$$\{ \langle u \rangle \} = \langle v \rangle = 0. \quad (3.26)$$

The dependent variables will be expressed as a combination of a basic and a disturbance part as follows:

$$u(x, y, z, t) = U_d(x, y) + u'(y, z, t), \quad (3.27)$$

$$v(x, y, z, t) = V_d(x, y) + v'(y, z, t), \quad (3.28)$$

$$w(y, z, t) = w'(y, z, t), \quad (3.29)$$

$$\theta(y, z, t) = \theta'(y, z, t), \quad (3.30)$$

$$\varphi(x, y, z, t) = \Phi(x, y) + \varphi'(y, z, t), \quad (3.31)$$

where the quantities with primes represent the disturbance part of the variables.

The basic wind field that drives the frontogenesis is the nondivergent and irrotational deformation field given by

$$U_d(x, y) = -\frac{D_d}{\mu} \sinh(\mu x) \sin(\mu y), \quad (3.32)$$

$$V_d(x, y) = -\frac{D_d}{\mu} \cosh(\mu x) \cos(\mu y). \quad (3.33)$$

This wind deformation field was originally used by Stone (1966) in his study of quasi-geostrophic frontogenesis.

It has been assumed that the perturbations are independent of x . If the expressions for u and v (3.27 and 3.28 respectively) are substituted into the basic equations, $\frac{\partial u}{\partial t}$ and $\frac{\partial v}{\partial t}$ will be functions of x . In this study, where the main interest is in examining cross front variations, the equations will be evaluated at $x = 0$. This will make the mathematical formulations compatible with the previous assumptions and it is expected that the results will be physically consistent.

Therefore, the basic wind deformation field will become

$$U_d(0,y) = 0, \quad (3.34)$$

$$V_d(0,y) = -\frac{Dd}{\mu} \cos \mu y. \quad (3.35)$$

The basic geopotential field Φ is chosen such that it will be in geostrophic balance with the wind deformation field as follows:

$$fU_d = -\frac{\partial \Phi}{\partial y}, \quad (3.36)$$

$$-fV_d = -\frac{\partial \Phi}{\partial x}. \quad (3.37)$$

Substitution of (3.36) and (3.37) into (3.27) and (3.28) respectively, and use of the expressions obtained for the dependent variables in equations (3.1)-(3.4) yields the following set:

$$\frac{du}{dt} = fv, \quad (3.38)$$

$$\frac{dv}{dt} = -\frac{\partial \varphi}{\partial y} - fu - (v + V_d) \frac{\partial V_d}{\partial y}, \quad (3.39)$$

$$\frac{\partial v}{\partial y} + \frac{\partial w}{\partial z} = 0, \quad (3.40)$$

$$\frac{d\theta}{dt} = 0. \quad (3.41)$$

where the primes were dropped from the disturbance variables.

Finally, an easier way to obtain $\frac{\partial \varphi}{\partial y}$ will be described. The dependent variable φ can be expressed as

$$\varphi = \varphi_0 + \varphi_s, \quad (3.42)$$

where

$$\varphi_s = \int_0^z \frac{g\theta}{\theta_0} dz. \quad (3.43)$$

Differentiate (3.42) with respect to y , to obtain

$$\frac{\partial \varphi}{\partial y} = \frac{\partial \varphi_0}{\partial y} + \frac{g}{\theta_0} \int_0^z \frac{\partial \theta}{\partial y} dz. \quad (3.44)$$

The value of φ_0 is not known, by virtue of the rigid lid assumption. In practice v will be predicted using equation (3.44) with $\frac{\partial \varphi_0}{\partial y}$ assumed initially equal to zero. After that, the v field will be adjusted in order to satisfy $\langle v \rangle = 0$. This procedure will be equivalent to solving equations (3.11) and (3.17) for φ , differentiating the values obtained with respect to y , and substituting into (3.39). Equations (3.38)-(3.41) and (3.44) give a complete set that can be integrated in time in order to predict the values of the dependent variables.

IV. NUMERICAL SOLUTION

A. INITIAL CONDITIONS

The initial conditions used in this model are similar to the ones used by Williams et al.(1991) in their study of effects of topography on fronts.

The initial temperature field is given by

$$\theta(y,z,0) = \frac{\partial\theta_s}{\partial z} \left[z - \frac{H}{2} \right] - e \quad (4.1)$$

where

$$e = A \cos(\mu y) \cos^2 \left[\left(\frac{z}{z_t} \right) \frac{\pi}{2} \right], \quad z \leq z_t \quad (4.2)$$

$$e = 0, \quad z > z_t \quad (4.3)$$

In the expression above $\frac{\partial\theta_s}{\partial z}$ is a constant. A is the amplitude of the temperature disturbance and z_t is the height of the upper limit where the temperature disturbance is present. This initial temperature field will confine the frontogenesis to the lower layers of the atmosphere, which will make the results more realistic.

The initial u component field is chosen to be in thermal wind balance with the temperature field and is given by

$$u(y, z, 0) = -\frac{g\mu A}{2f\theta_0} \sin(\mu y) \cdot \lambda \quad (4.4)$$

where

$$\lambda = (z - z_r) - \frac{z_r}{\pi} \sin \left[\left(\frac{z - z_r}{z_r} \right) \pi \right], \quad z \leq z_r \quad (4.5)$$

$$\lambda = 0, \quad z > z_r \quad (4.6)$$

and the condition

$$u(y, z_r, 0) = 0 \quad (4.7)$$

has been used.

The initial v and w fields are obtained from the solution of the quasi-geostrophic circulation equation (Williams, 1972)

$$\frac{g}{f^2 \theta_0} \frac{\partial \theta_s}{\partial z} \frac{\partial^2 \psi}{\partial y^2} + \frac{\partial^2 \psi}{\partial z^2} = - \frac{2g}{f^2 \theta_0} \frac{\partial V_d}{\partial y} \frac{\partial \theta}{\partial y}, \quad (4.8)$$

where

$$v = - \frac{\partial \psi}{\partial z} \quad (4.9)$$

$$w = \frac{\partial \psi}{\partial y} \quad (4.10)$$

The vertical boundary conditions for the solution of (4.8) are set to

$$\psi(z = 0) = \psi(z = H) = 0 \quad (4.11)$$

It can be shown, from the domain averaging of equation (4.2) that $\langle u \rangle$ will be zero initially. Also, the condition (4.11) will allow (3.25) and (3.26) to be satisfied in order for the numerical solution to be consistent with the assumptions of the model.

B. THE SPATIAL GRID

The numerical calculations are performed on a staggered grid, both in the horizontal and in the vertical directions. In the horizontal the variables are staggered following the scheme B described in Arakawa and Lamb (1977). This scheme, as shown in Haltiner and Williams (1980), allows a better representation of geostrophic adjustment processes. The variables are also staggered in the vertical. Pielke (1984) points out that the staggering of the u and w components in the vertical gives better solutions for the vertical velocity from the continuity equation.

The horizontal grid uses I grid points separated by a constant grid space Δy . The vertical grid has K grid points and also uses a constant grid spacing, referred to as Δz . Figure 1 shows the arrangement of the variables on the grid.

C. FORMULATION OF THE MODELS

1. Semi-Lagrangian Explicit Scheme

In the semi-Lagrangian explicit formulation of the present model, the total derivatives will be approximated using the technique described in chapter II. The remaining terms of the equations are evaluated at the positions of the fluid particles at time level t . Introducing those approximations into the prognostic equations (3.38), (3.39) and (3.41) the following set is obtained, after dropping subscripts i and j :

$$\frac{u(y, z, t + \Delta t) - u(y - 2a, z - 2b, t - \Delta t)}{2\Delta t} = f.v(y - a, z - b, t), \quad (4.12)$$

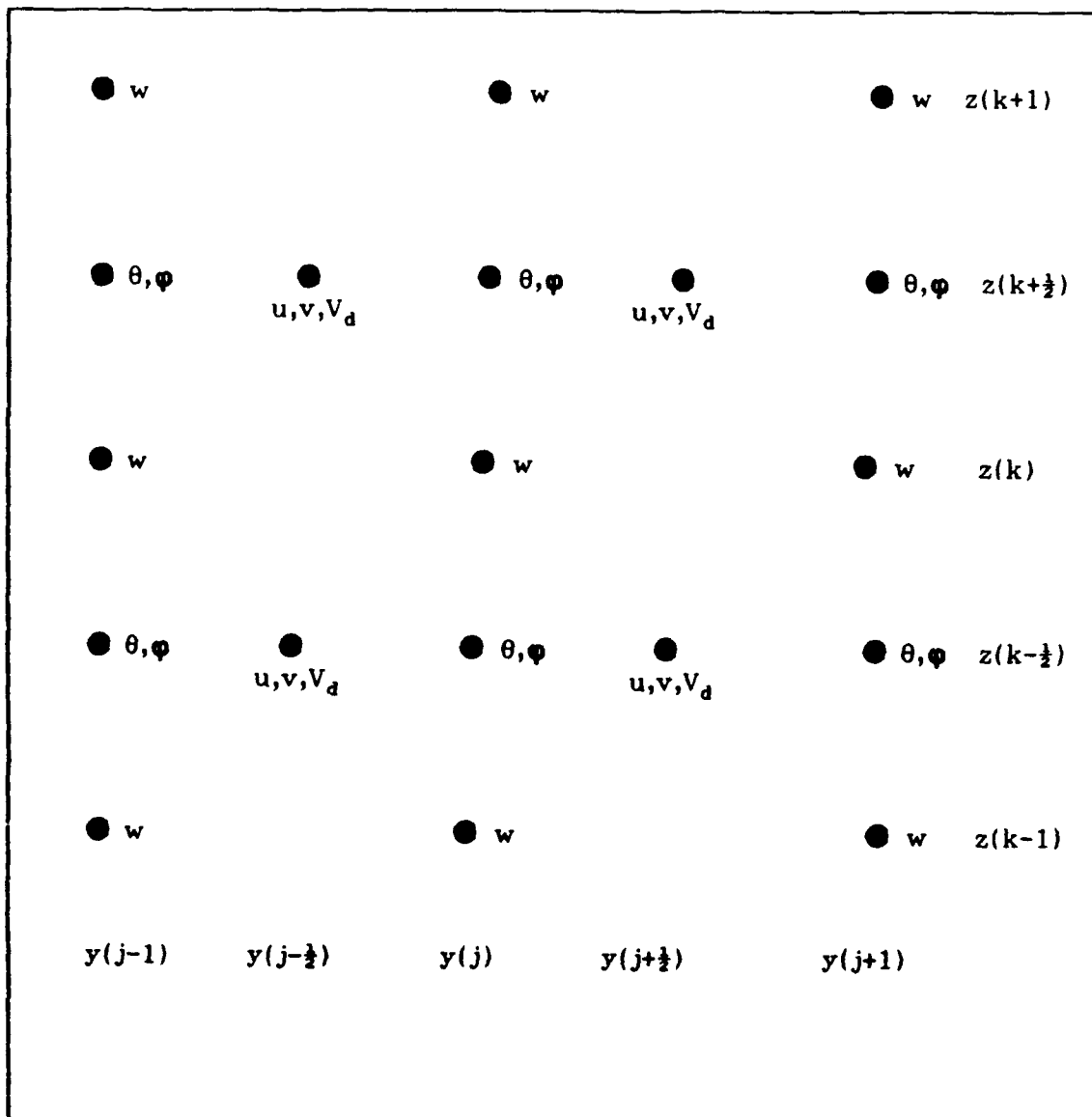


Figure 1: Staggered spatial grid

$$\frac{v(y, z, t + \Delta t) - v(y - 2a, z - 2b, t - \Delta t)}{2\Delta t} -$$

$$- \frac{\partial \phi}{\partial y}(y - a, z - b, t) - f \cdot u(y - a, z - b, t)$$

$$- [v(y - a, z - b, t) + V_d(y - a)] \frac{\partial V_d}{\partial y}(y - a), \quad (4.13)$$

$$\frac{\theta(y, z, t + \Delta t) - \theta(y - 2a, z - 2b, t - \Delta t)}{2\Delta t} = 0. \quad (4.14)$$

The values of w and ϕ are obtained from the diagnostic equations (3.40) and (3.45), respectively.

2. Semi-Lagrangian Semi-Implicit Scheme

The semi-Lagrangian semi-implicit scheme was introduced in this model following the development described by Robert et al.(1985). The scheme consists of separating the temperature into a basic state, dependent only on the vertical coordinate z , and a disturbance part. Next, an implicit treatment is given to those terms related to gravity waves, namely: horizontal pressure gradient, divergence and vertical motion.

To obtain the system of equations in the semi-implicit formulation take the advective terms out of the total derivatives in equations (3.38), (3.39) and (3.44);

$$\frac{d_H u}{dt} + w \frac{\partial u}{\partial z} = f v, \quad (4.15)$$

$$\frac{d_H v}{dt} + w \frac{\partial v}{\partial z} = - \frac{\partial \phi}{\partial y} - f u - (v + V_d) \frac{\partial V_d}{\partial y}, \quad (4.16)$$

$$\frac{d_H \theta}{dt} + w \frac{\partial \theta}{\partial z} = 0, \quad (4.17)$$

where the terms with subscript H represent horizontal components of the total derivative.

Replace the temperature and geopotential fields by basic state and disturbance parts as follows:

$$\theta(y, z, t) = \theta^*(z) + \theta'(y, z, t), \quad (4.18)$$

$$\phi(y, z, t) = \phi^*(z) + \phi'(y, z, t), \quad (4.19)$$

where the superscripts (*) represent the basic state parts of the variables.

Now introduce (4.18) and (4.19) into equations (3.5), (3.40) and (4.15)-(4.17), and take the time average of those terms related to gravity waves, which yields

$$\frac{d_H u}{dt} + w \frac{\partial u}{\partial z} = fv, \quad (4.20)$$

$$\frac{d_H v}{dt} + w \frac{\partial v}{\partial z} = -\frac{\partial \bar{\phi}'}{\partial y} - fu - (v + V_d) \frac{\partial V_d}{\partial y}, \quad (4.21)$$

$$\frac{\partial \bar{v}}{\partial y} + \frac{\partial \bar{w}}{\partial z} = 0, \quad (4.22)$$

$$\frac{d_H \theta'}{dt} + w \frac{\partial \theta'}{\partial z} + w \frac{\partial \theta^*}{\partial z} = 0, \quad (4.23)$$

$$\frac{\partial \phi^*}{\partial z} = \frac{g \theta^*}{\theta^0}, \quad (4.24a)$$

$$\frac{\partial \phi'}{\partial z} = \frac{g \theta'}{\theta_0}, \quad (4.24b)$$

where $(\bar{\quad})$ denotes the time average operator.

Define the explicit terms at time t as

$$r_1 = w \frac{\partial u}{\partial z} - fv, \quad (4.25)$$

$$r_2 = w \frac{\partial v}{\partial z} + fu + (v + V_d) \frac{\partial V_d}{\partial y}, \quad (4.26)$$

$$r_3 = w \frac{\partial \theta'}{\partial z}. \quad (4.27)$$

Using (4.25)-(4.27) in (4.20)-(4.23), the following set of equations is obtained:

$$\frac{d_H u}{dt} + r_1 = 0, \quad (4.28)$$

$$\frac{d_H v}{dt} + \frac{\partial \bar{\phi}}{\partial y} + r_2 = 0, \quad (4.29)$$

$$\frac{\partial \bar{v}}{\partial y} + \frac{\partial \bar{w}}{\partial z} = 0, \quad (4.30)$$

$$\frac{d_H \theta'}{dt} + \bar{w} \frac{\partial \theta^*}{\partial z} + r_3 = 0. \quad (4.31)$$

Next, define the auxiliary variables

$$F^+ = F(y, z, t + \Delta t), \quad (4.32a)$$

$$F^0 = F(y - a, z, t), \quad (4.32b)$$

$$F^- = F(y - 2a, z, t - \Delta t), \quad (4.32c)$$

where

$$a^{n+1} = \Delta t \cdot (v^0(y - a^n, t) + V_d^0(y - a^n, t)). \quad (4.33)$$

Note that the use of the time average of the vertical velocity w eliminates the need of considering vertical displacements in the calculation of the trajectories of the

fluid particles. Therefore, the interpolation will be performed only in the horizontal direction using one dimensional cubic spline functions.

Define the following approximations for the time derivatives and time average respectively:

$$\frac{d_H F}{dt} = \frac{F^+ - F^-}{2\Delta t}, \quad (4.34)$$

$$\bar{F} = \frac{F^+ + F^-}{2}, \quad (4.35)$$

Use of approximations (4.34) and (4.35) into (4.28)-(4.31) gives

$$\frac{u^+ - u^-}{2\Delta t} + r_1 = 0, \quad (4.36)$$

$$\frac{v^+ - v^-}{2\Delta t} + \frac{1}{2} \left(\frac{\partial \phi^+}{\partial y} + \frac{\partial \phi^-}{\partial y} \right) + r_2 = 0, \quad (4.37)$$

$$\frac{\partial v^+}{\partial y} + \frac{\partial w^+}{\partial z} = 0, \quad (4.38a)$$

$$\frac{\partial v^-}{\partial y} + \frac{\partial w^-}{\partial z} = 0, \quad (4.38b)$$

$$\frac{\theta^+ - \theta^-}{2\Delta t} + \frac{1}{2} \frac{\partial \theta^*}{\partial z} (w^+ + w^-) + r_3 = 0. \quad (4.39)$$

Group the terms at time $(t-\Delta t)$ and define new auxiliary variables p_i :

$$p_1 = -u^-, \quad (4.40)$$

$$p_2 = -v^- + \Delta t \frac{\partial \phi'^-}{\partial y}, \quad (4.41)$$

$$p_3 = -\theta' + \Delta t \frac{\partial \theta^*}{\partial z} w^-. \quad (4.42)$$

Similarly, group the terms at time $(t + \Delta t)$ and define the auxiliary variables

q_i :

$$q_1 = u^* , \quad (4.43)$$

$$q_2 = v^* + \Delta t \frac{\partial \phi'^*}{\partial y} , \quad (4.44)$$

$$q_3 = \theta'^* + \Delta t \frac{\partial \theta^*}{\partial z} w^* . \quad (4.45)$$

Use of (4.40)-(4.45) allows to rewrite (4.36), (4.37) and (4.39) as follows:

$$q_1 = -p_1 - 2 \Delta t r_1 , \quad (4.46)$$

$$q_2 = -p_2 - 2 \Delta t r_2 , \quad (4.47)$$

$$q_3 = -p_3 - 2 \Delta t r_3 . \quad (4.48)$$

The variables p_i and r_i can be calculated explicitly and with their values the q_i variables can be obtained.

To calculate the values of the variables u , v , w , θ and ϕ at the time level $(t + \Delta t)$ it is necessary to solve the system of equations composed by (4.38b), (4.43)-(4.45) and the hydrostatic equation (4.24b). The procedure used by Robert et al. (1985) consists of first solving an elliptic equation for ϕ .

In this model it is not possible to state exact boundary conditions for ϕ , due to the use of the rigid lid assumption. However, the w field has the exact boundary conditions (3.13). The following elliptic equation for w can be derived from the system of equations at time level $(t + \Delta t)$:

$$\frac{\partial^2 w^*}{\partial z^2} + \frac{\Delta t^2 g}{\theta_0} \frac{\partial \theta^*}{\partial z} \frac{\partial^2 w^*}{\partial y^2} = \frac{\Delta t g}{\theta_0} \frac{\partial^2 q_3}{\partial y^2} + \frac{\partial^2 q_2}{\partial y \partial z}. \quad (4.49)$$

Once w^* was calculated, θ was determined using (4.45), and $\frac{\partial \phi'}{\partial y}$ and v were obtained using the procedure described in Chapter III. After adjusting the v field to satisfy $\langle v \rangle = 0$, a new $\frac{\partial \phi'}{\partial y}$ field was calculated using the new values of v in (4.44) and the w field was also adjusted to satisfy the continuity equation (4.38a).

Finally, both in the explicit and the semi-implicit schemes the spatial derivatives are approximated by centered in space finite differences. Following Monk (1989), the derivatives are first evaluated at the grid points and, after that the values are interpolated for the position of the fluid particle. This procedure is computationally more efficient than the calculation of the derivatives at the fluid particle points, which would double the number of interpolations.

V. EXPERIMENTS AND RESULTS

A. PARAMETERS USED IN THE EXPERIMENTS

The following values for the constants were used in all experiments:

$$L = 3600 \text{ km,}$$

$$H = 12 \text{ km,}$$

$$A = 12^\circ \text{ K,}$$

$$\theta_0 = 300^\circ \text{ K,}$$

$$g = 9.81 \text{ m s}^{-2},$$

$$f = 10^{-4} \text{ s}^{-1},$$

$$D_d = 10^{-5} \text{ s}^{-1},$$

$$z_t = 9 \text{ km,}$$

$$\frac{\partial \theta}{\partial z} = 4^\circ \text{ K km}^{-1}.$$

For the semi-Lagrangian semi-implicit (SLSI) case there were two control runs using $\Delta y = 20 \text{ km}$ and $\Delta z = 167 \text{ m}$. All the remaining experiments used normal resolution, with $\Delta y = 40 \text{ km}$ and $\Delta z = 333 \text{ m}$. The cross-sections of the initial fields are shown in Figs. 2-5. There is a warm front with thermally indirect circulation near $y = 900 \text{ km}$ and a cold front with thermally direct circulation near $y = 2700 \text{ km}$.

In order to assess the evolution of the frontogenesis process, the following parameter is defined at the lowest computational level:

$$d = \frac{|\Delta \theta|}{\left| \frac{\partial \theta}{\partial y} \right|_{\max}}, \quad (5.1)$$

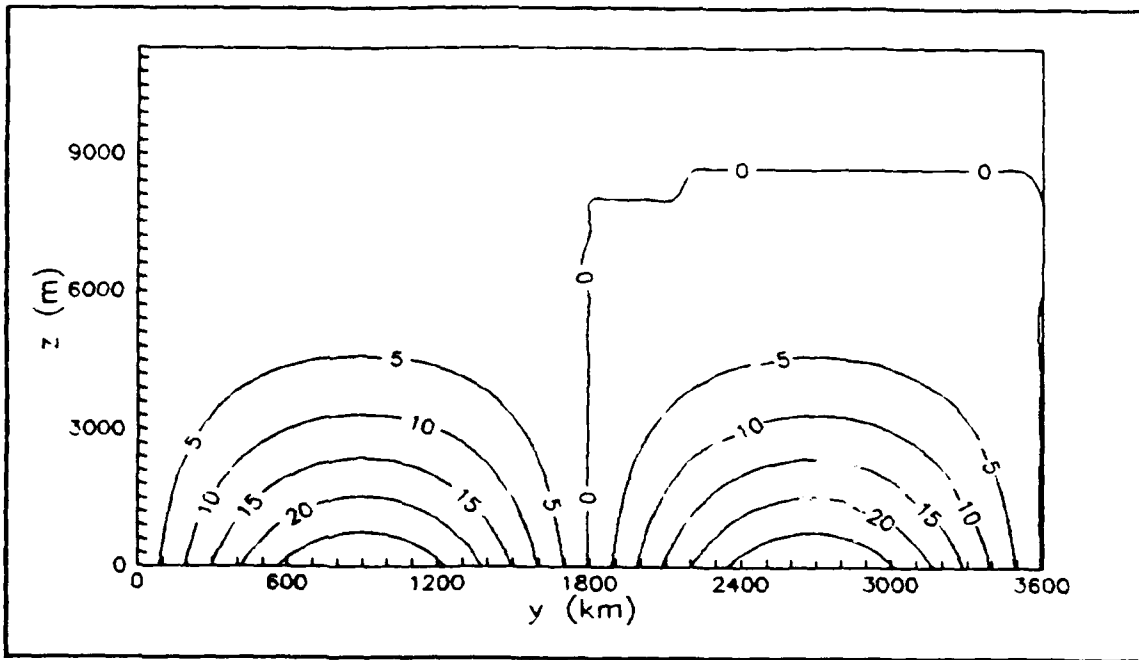


Figure 2. Initial u component field (m/s).

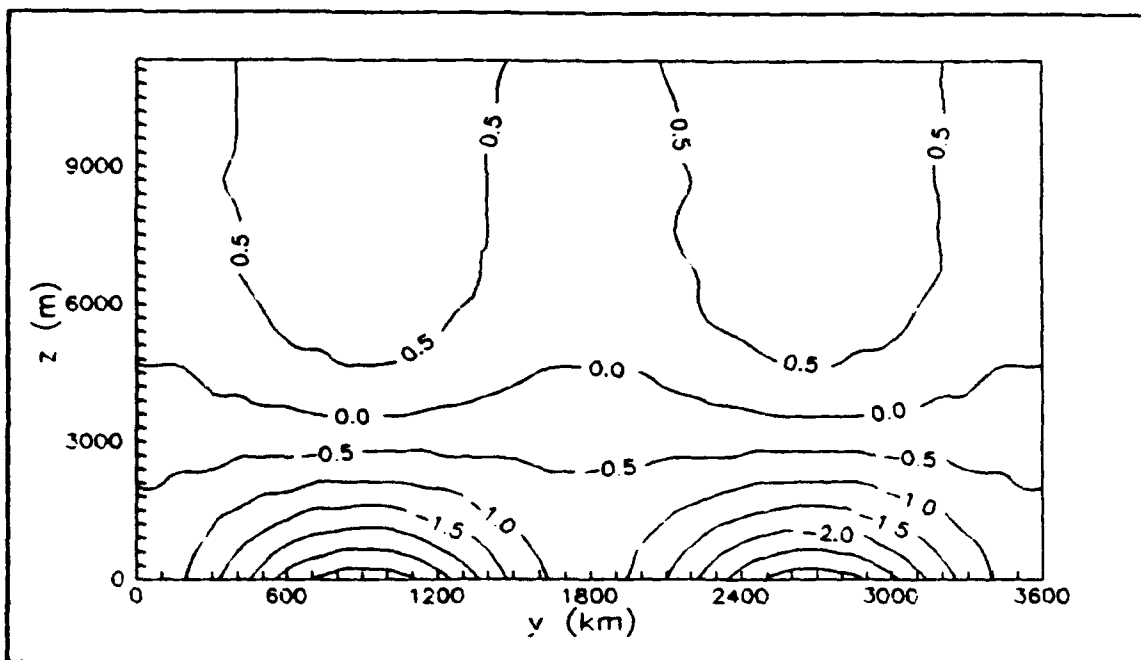


Figure 3. Initial v component field (m/s).

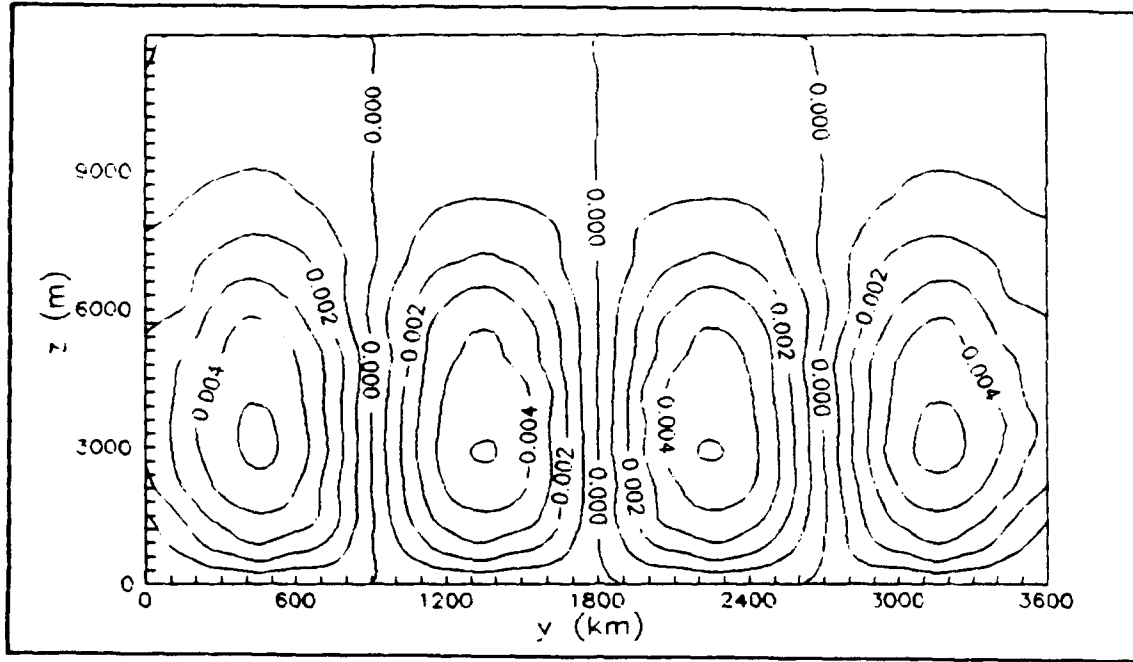


Figure 4. Initial w component field (m/s).

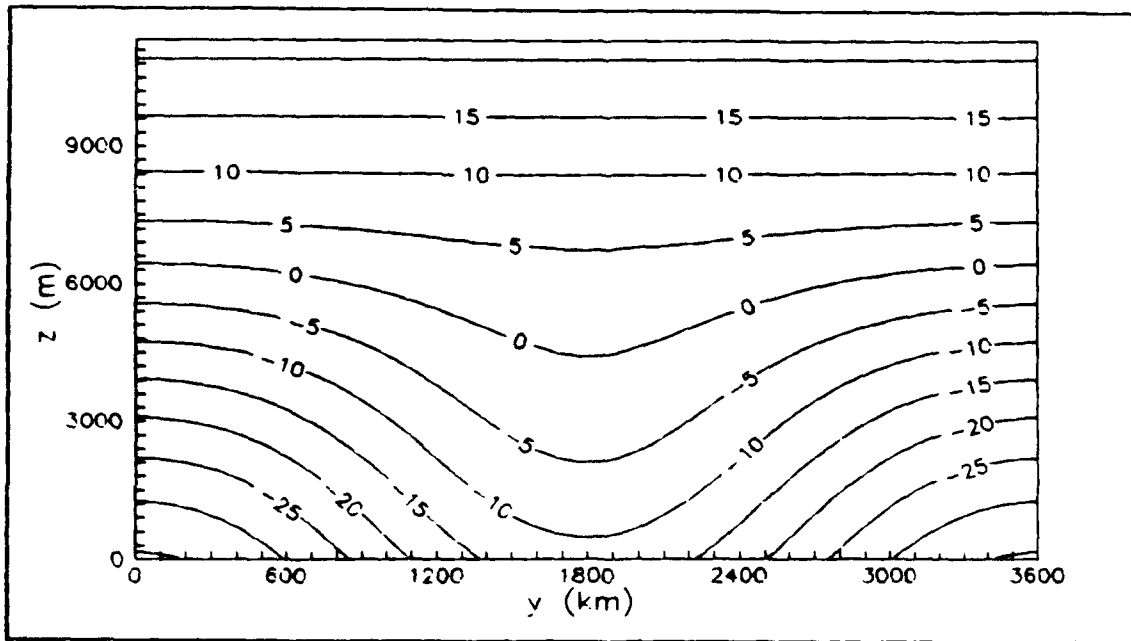


Figure 5. Initial θ field ($^{\circ}\text{K}$).

where $\Delta\theta$ is the maximum variation of θ along the y direction. This parameter, used by Williams et al.(1991), gives a reasonable measure of the width of the frontal zone.

During the first experiment with the semi-implicit scheme, a high frequency oscillation was observed in the frontal width. That noise was not present in the experiments carried out with the semi-Lagrangian explicit (SLEX) scheme. In order to eliminate the noise, a time filtering technique similar to the one described by Asselin (1972) was used. The time filtering of a variable Q is defined as

$$\overline{\overline{Q(t)}} = Q(t) + \gamma [Q(t + \Delta t) - 2Q(t) + \overline{\overline{Q(t - \Delta t)}}], \quad (5.2)$$

where $Q(t + \Delta t)$ has been previously obtained by using the respective predictive equation with the unaveraged value of $Q(t)$. The time filter defined above is expected to affect the higher frequencies only.

Several experiments were performed with the objective of assessing how the use of time filtering would affect the solutions, as will be described next.

B. DESCRIPTION OF THE EXPERIMENTS

The experiments basically consisted of carrying out time integrations of the model using the SLEX and SLSI schemes, starting from the same initial conditions and using different combinations of time step Δt and filtering factor γ . The experiments were intended to give information about the following points:

- How well the different schemes handle the formation of large gradients;
- How the use of time filtering affects the final solutions; and
- How the solutions are affected by the use of longer time steps.

Table 1 shows the experiments performed with the SLEX scheme, as a function of time step Δt and filtering factor γ . The experiments carried out using the SLSI scheme are identified on Table 2.

TABLE 1. EXPERIMENTS WITH THE SLEX SCHEME.

Δt (sec.)	$\gamma = 0.0$	$\gamma = 0.01$	$\gamma = 0.03$
180	SLEX01	SLEX02	SLEX03
360	SLEX04	SLEX05	SLEX06
600	SLEX07	---	SLEX08

TABLE 2. EXPERIMENTS WITH THE SLSI SCHEME.

Δt (sec.)	$\gamma = 0.0$	$\gamma=0.01$	$\gamma=0.03$	$\gamma=0.05$	$\gamma=0.07$	$\gamma=0.1$
180	SLSI01	SLSI02	SLSI03	SLSI23	---	---
360	SLSI04	SLSI05	SLSI06	SLSI24	---	---
600	SLSI07	SLSI08	SLSI09	SLSI25	---	---
1200	---	SLSI10	SLSI11	SLSI12	---	---
1800	---	SLSI13	SLSI14	SLSI15	---	---
2400	---	SLSI16	SLSI17	SLSI18	SLSI19	---
3600	---	SLSI20	SLSI21	SLSI22	SLSI26	SLSI27

There were two high-resolution experiments, both using the SLSI scheme, with time steps of 180 secs. In the first of them, identified by SLHR01, the time filtering factor $\gamma = 0.01$ was used, and in the second one (SLHR02) γ was set equal to 0.05. The velocity components and temperature fields at time $t = 40$ hours, for experiment SLHR01 are shown in Figs. 6-9. The occurrence of frontogenesis for the surface cold front and frontolysis for the warm front can be seen. These processes are due to the relation between the wind deformation and temperature disturbance fields, that gives convergence in the cold front region and divergence for the warm front. The w and v fields give a direct circulation around the cold frontal zone and an indirect circulation about the warm frontal zone. The u field develops cyclonic shear at the cold front.

The evolution of the frontal width (*d-value*) for SLHR01 is presented in Fig. 10. An almost linear decrease in the frontal scale can be seen. This curve is different from that obtained by Williams et al.(1991), because in that case there was a momentum diffusion term that gave an asymptotic behavior in the evolution of the frontal width towards a balance condition. In the present model a continuous reduction of the frontal scale is expected until a limit, when the grid resolution is reached. Figure 11 shows the evolution of the *d-value* for experiment SLEX01. It can be seen that the minimum value of the frontal width is reached at approximately $t = 40$ hours. Note that this curve is more linear than that obtained in experiment SLHR01. Also, the *d-value* curves obtained for experiments SLEX02 and SLEX03 were virtually coincident with the one for SLEX01. This result shows that the use of stronger filtering effect (larger γ) does not affect the evolution of the frontogenesis process represented by the SLEX scheme.

During the first experiment with the SLSI scheme (SLSI01) the *d-value* curve, shown in Fig. 12, presented a high frequency oscillation. The time integration could be carried out until time $t = 36$ hours and after that, the iterative procedures no longer

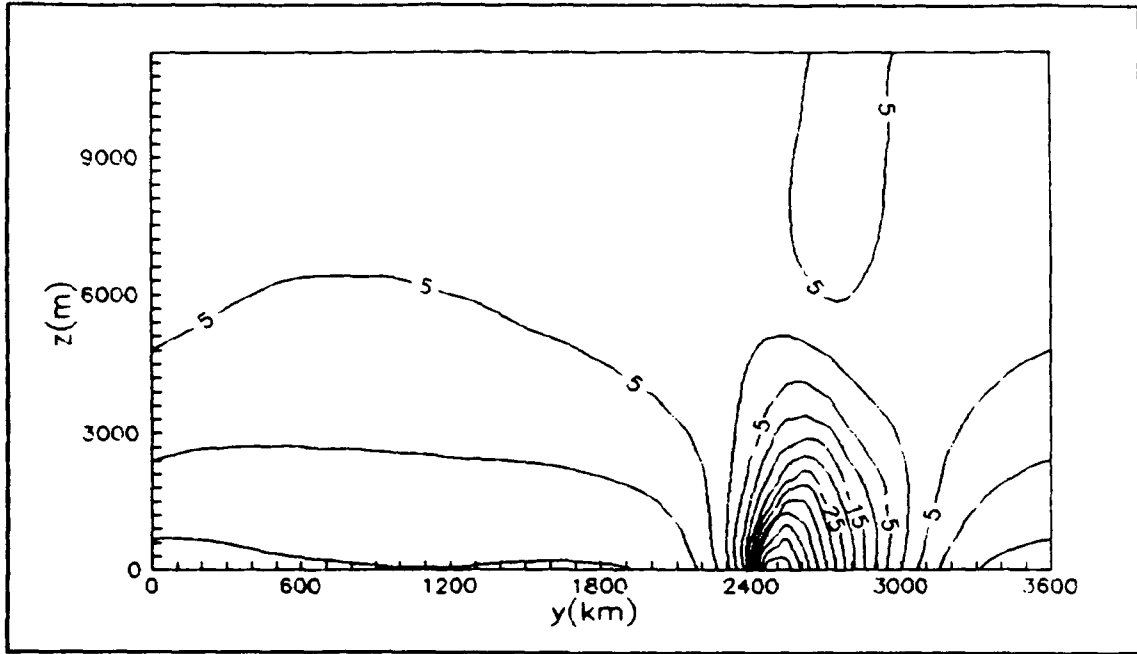


Figure 6. u component field (m/s) for SLHR01 at $t = 40$ hours.

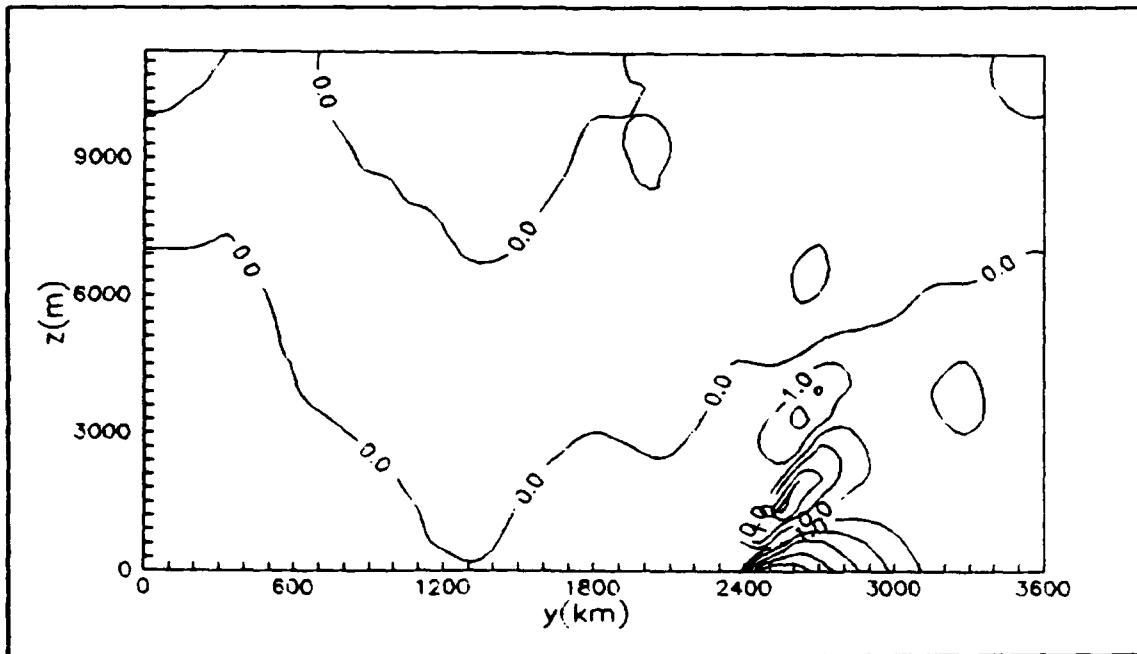


Figure 7. v component field (m/s) for SLHR01 at $t = 40$ hours.

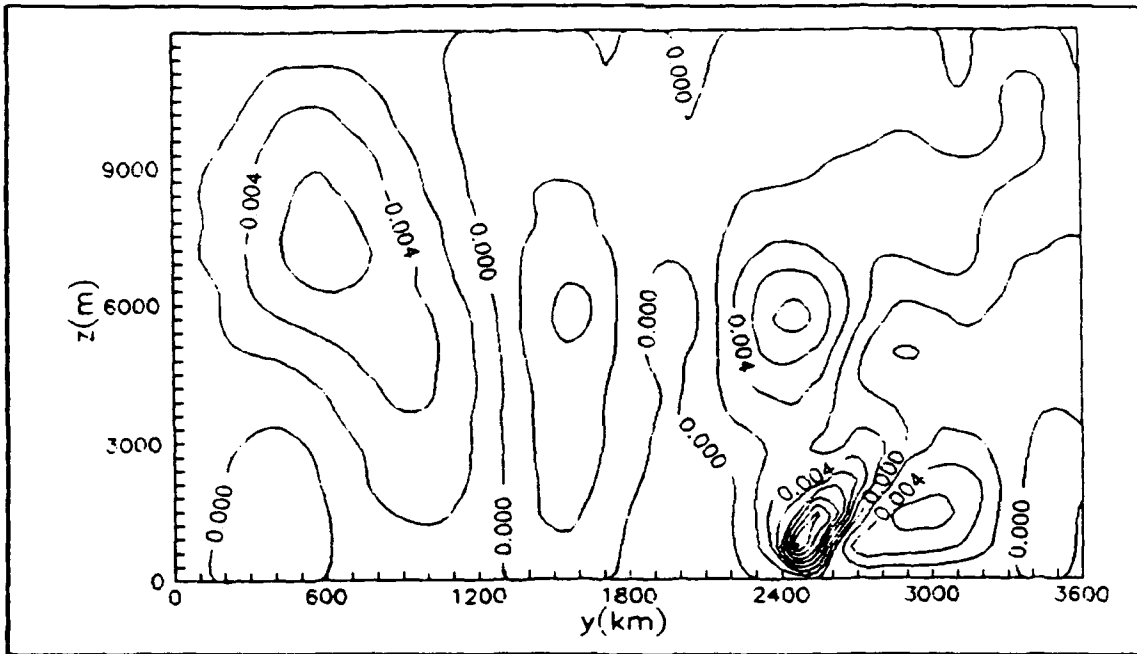


Figure 8. w component field (m/s) for SLHR01 at $t = 40$ hours.

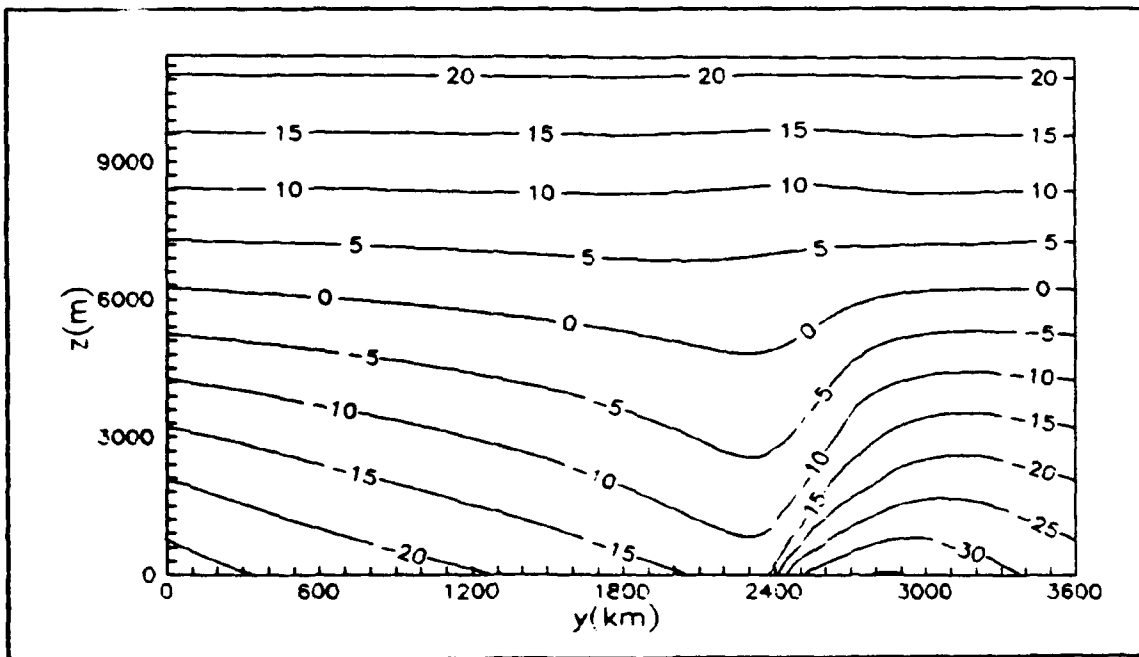


Figure 9. θ field ($^{\circ}\text{K}$) for SLHR01 at $t = 40$ hours.

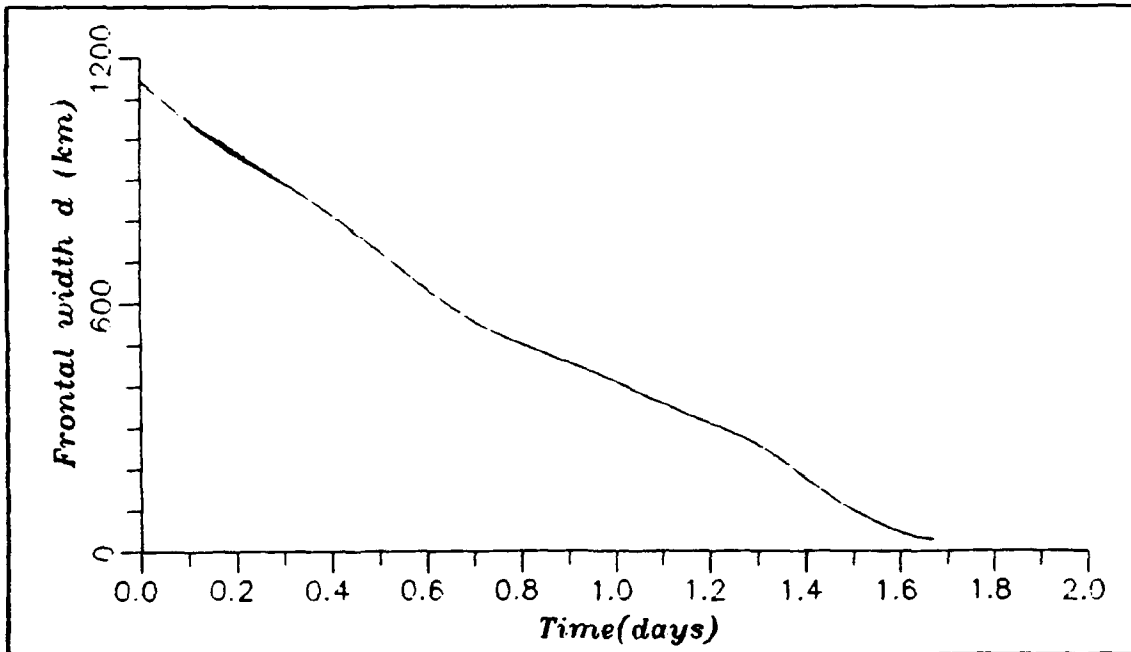


Figure 10. Evolution of the frontal width (d-value) for SLHR01.

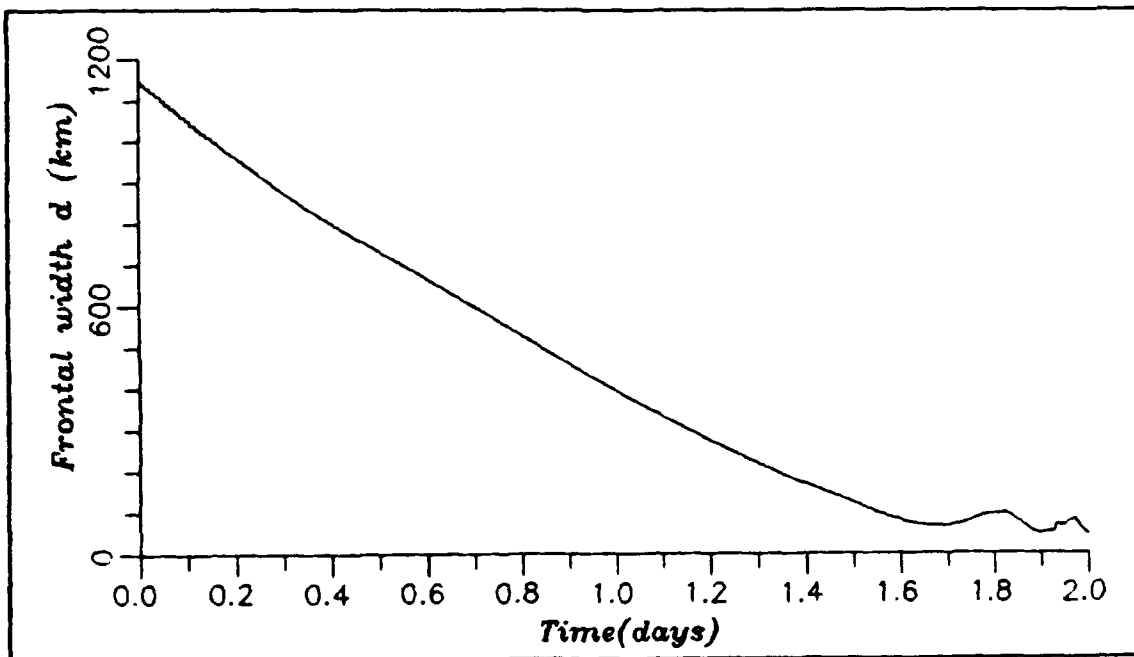


Figure 11. Evolution of the frontal width (d-value) for SLEX01.

achieved convergence and the integration was terminated. It is important to note that the irregular behavior of the curve was not related to continuous amplification of the solution due to numerical instability and that the curve presents a general tendency to the frontogenesis solution obtained in the SLEX experiments. The high resolution experiment SLHR01 also shows a low frequency oscillation about its linear decrease in d .

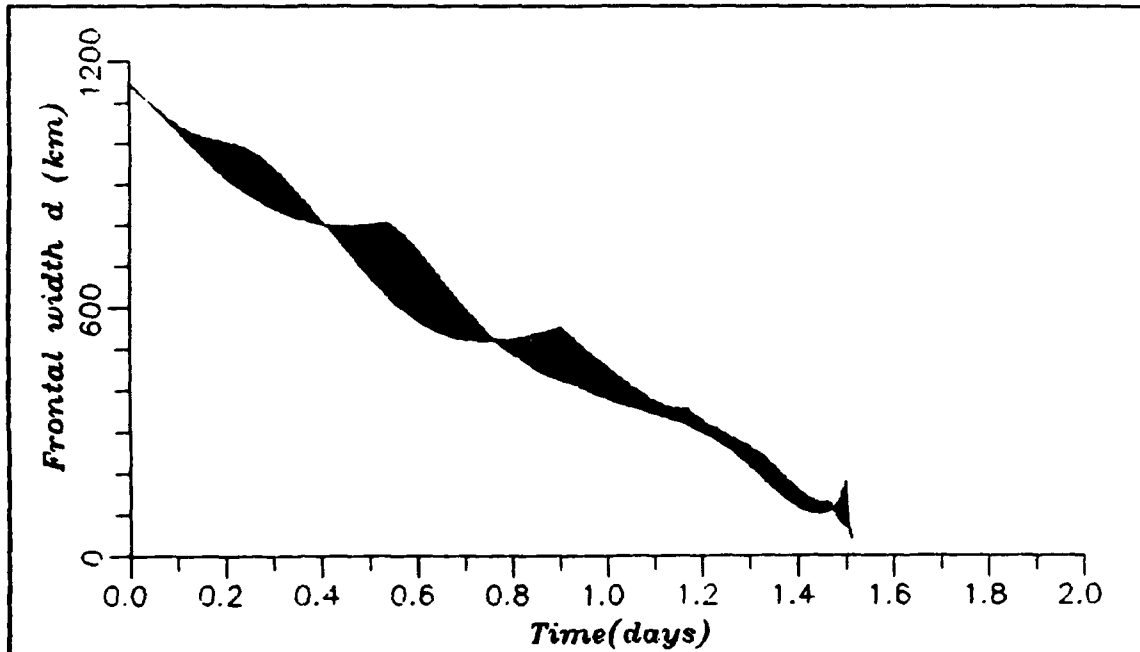


Figure 12. Evolution of the frontal width (d -value) for SLSI01.

In order to eliminate the noise the time filter described in the last section was introduced. Figure 13 shows the evolution of the frontal width obtained in experiment SLSI02, with the filtering factor γ set equal to 0.01. It can be seen from the figure that although the filtering effect was small, it was adequate to suppress the high frequency oscillations.

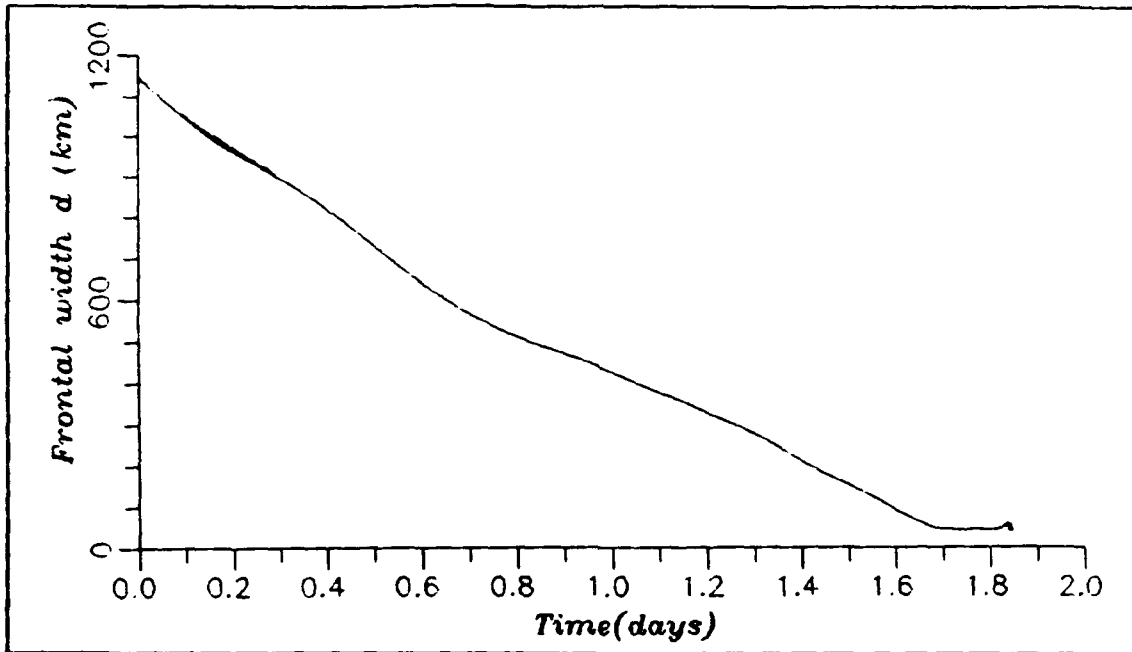


Figure 13. Evolution of the frontal width (*d*-value) for experiment SLSI02.

Figures 11 and 13 show that both for the the SLSI and SLEX experiments the minimum frontal width is reached approximately at time $t = 40$ hours and after that the *d*-value curves oscillate. Those oscillations can be related to the fact that the front reached a width corresponding to the model resolution and after that point the solutions were no longer physically consistent.

Tables 3 and 4 show the minimum value of the frontal width for the SLEX experiments with time steps 180, 360 and 600 sec., and the corresponding SLSI experiments for which the time integrations could be carried out until $t = 40$ hours. Also presented is the time when the minimum *d*-value occurred.

Comparison of the values presented in Tables 3 and 4 show that the minima *d*-values obtained in the SLSI experiments are smaller than those obtained for the corresponding SLEX experiments with same Δt and γ . Also, in the SLEX experiments the minimum frontal width increases as Δt increase whereas in the SLSI case there is no

significant change in the minimum *d-value* due to changes in the time step. It is interesting to note that for the SLEX case a shorter time integration is necessary for the minimum to occur for increasing time step, while the inverse tendency is observed in the SLSI case that is, a longer time integration is necessary for the minimum frontal width to occur, for larger Δt .

TABLE 3. MINIMUM D-VALUE FOR SLEX EXPERIMENTS.

Δt (sec.)	γ	Experiment	Minimum d-value (km)	Time (hour)
180	0.0	SLEX01	49.0	45.5
180	0.01	SLEX02	49.0	45.5
180	0.03	SLEX03	49.0	45.5
360	0.0	SLEX04	68.4	39.6
360	0.01	SLEX05	68.3	39.9
360	0.03	SLEX06	68.3	39.6
600	0.0	SLEX07	69.9	39.3
600	0.03	SLEX08	69.8	39.5

Therefore, it can be concluded that the SLSI scheme gives a better representation of the scale collapse process than that obtained from the SLEX scheme, since narrower frontal widths can be resolved by the former than by the latter.

TABLE 4. MINIMUM D-VALUE FOR SLSI EXPERIMENTS.

Δt (sec.)	γ	Experiment	Minimum d-value (km)	Time (hours)
180	0.01	SLSI02	43.4	41.5
180	0.03	SLSI03	43.4	41.7
360	0.01	SLSI05	43.4	41.5
360	0.03	SLSI06	43.4	42.0
600	0.03	SLSI09	43.1	42.0

Experiment SLSI03 used $\gamma = 0.03$ and the *d-value* curve obtained was practically coincident with the one obtained in SLSI02, with $\gamma = 0.01$.

In experiments SLSI04 and SLSI07 no filtering was used ($\gamma = 0.0$) and approximately at time $t = 37$ hours the numerical integration was interrupted because the solutions were no longer able to achieve convergence in the iterative procedures. However, the use of larger values of γ (SLSI05, SLSI06, SLSI24, SLSI08, SLSI09, SLSI25) allowed the normal execution of the time integrations. Figure 14 shows the *d-value* curves for experiments SLSI08 and SLSI09. It can be seen that the oscillations were not completely filtered out with $\gamma = 0.01$ and a stronger filtering effect ($\gamma = 0.03$) was required. The experiments with longer time steps showed that as the time step increased a larger value for γ was required for an appropriate filtering of the noise. Also, all experiments with the SLSI scheme showed that the largest amplitudes of the noise occurred during the first 24 hours of integration. Furthermore, those experiments

showed that the noise was not related to imbalance in the initial conditions, since the mass and wind fields were initially adjusted using the quasi-geostrophic circulation equation (4.8) and the oscillations were not present before $t = 02$ hours. The presence of the noise was investigated by examining the u , v and θ fields obtained at the lowest computational level of experiment SLSI07. At time $t = 13$ hours, that corresponds approximately to maximum amplitude of the noise, there was no evidence of small scale spatial oscillations in those fields. Although the origin of the noise could not be determined, the experiments showed that the use of the time filter was effective in eliminating the oscillations with relatively small values of γ . It is expected that this filtering would not significantly affect the lower frequency solutions.

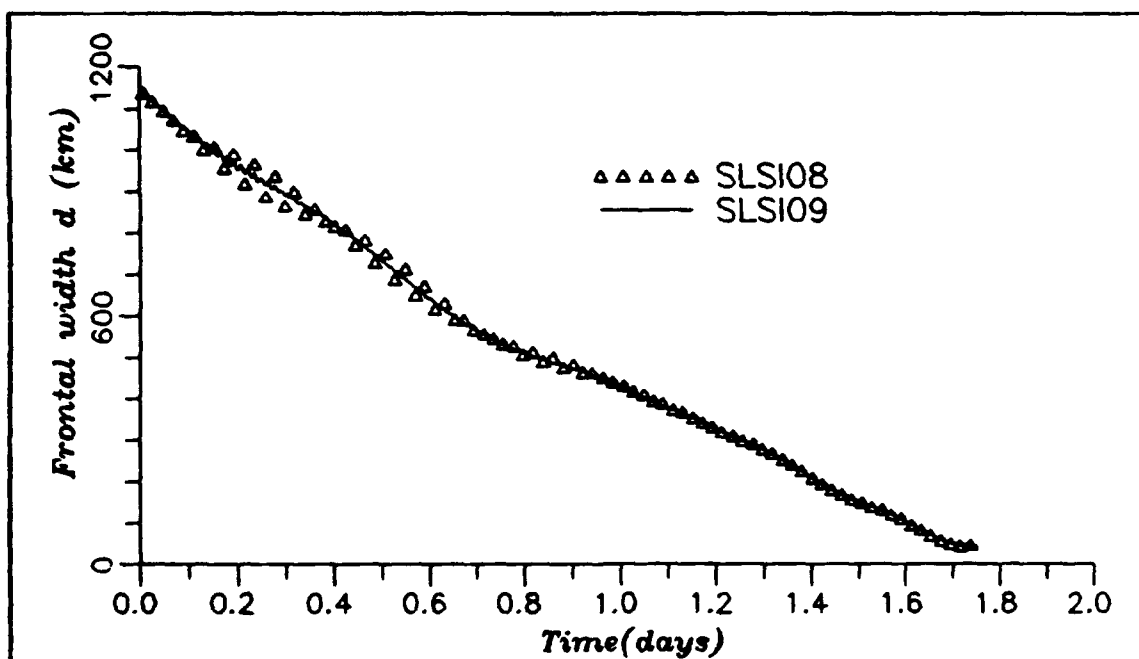


Figure 14. Evolution of the frontal width (d-value) for experiments SLSI08 and SLSI09.

Another point of interest in this study was the computational effort employed in each of the experiments, since one of the objectives of the SLSI scheme is to allow stable solutions with long time steps. In order to evaluate the relative computational

efficiency, the CPU time spent for running each experiment for 42 hours was measured and normalized by the CPU time used in SLSI01. It was observed that the CPU time was not affected by changes in the value of γ , so that the results are presented in Table 5 as a function of numerical scheme and time step only. As expected, the computational effort decreases almost linearly for increasing time step. Also, for a given time step, the SLEX scheme is more efficient than the SLSI one. This is observed because the SLSI technique requires the solution of an elliptic equation every time step. It should also be pointed out that in this study the SLSI formulation makes the spatial interpolations necessary only in the horizontal direction, whereas in the SLEX scheme the interpolations are performed using bicubic splines. Thus, a formulation of the SLSI scheme using two-dimensional interpolations could give a further increase in the computational effort. The advantage of the SLSI scheme appears clearly when integrations with time steps as long as 3600 sec. are performed with perfectly stable solutions, while the SLEX scheme did not allow time steps longer than 600 seconds.

In order to assess the accuracy of the several solutions, a second high resolution (SLHR02) control run was carried out with the SLSI scheme. The parameters used were $\Delta t = 180$ sec. and $\gamma = 0.05$. This value for γ was chosen to guarantee that the solutions would not be affected by noise. The solutions of the control run were linearly interpolated for the normal resolution grid point positions when necessary, because of the staggering of the variables. The differences between the values obtained for the control run and those obtained for the experiments with normal resolution were calculated at each grid point. The results were used to calculate the domain RMS differences for each variable. Two sets of comparisons were performed: In the first one the velocity components and temperature fields for selected SLSI experiments at $t = 36$ hours were compared with the ones obtained from SLHR02 at the same time. That

time was considered appropriate to give a well characterized atmospheric front and sufficiently away from the inconsistent solutions obtained after the model resolution was achieved.

TABLE 5. NORMALIZED CPU TIME FOR 42-HOUR MODEL INTEGRATION.

Δt (sec.)	SLEX	SLSI
180	0.84	1.00
360	0.42	0.50
600	0.25	0.30
1200	---	0.16
1800	---	0.11
2400	---	0.08
3600	---	0.06

The experiments chosen for this first set of comparisons were those with $\gamma = 0.05$ for all time steps, except $\Delta t = 3600$ sec., where $\gamma = 0.07$ was used. The accuracy of the solutions was expressed in terms of RMS differences in the values the of u, v, w and θ , given in Table 6.

The values obtained show that the v and θ fields have small errors as compared to the range of the values observed in the domain (-35 to $+22$ °K for θ and -50 to $+15$ $m s^{-1}$ for v). On the other hand, the errors obtained in the v and w fields were relatively large compared with the magnitude of the reference values obtained for SLHR02. The

large differences can be associated with the fact that the v and w components are closely related to the divergence in the model and their values can be significantly affected by the presence of gravity waves. Time series of v and w were examined and they confirmed the presence of internal gravity waves in the solutions. Thus, a single sample would not be sufficiently representative of the actual level of accuracy obtained in those fields.

TABLE 6. RMS DIFFERENCES FOR TIME T= 36 HOURS.

Experiment	Δt (sec.)	γ	u (m/s)	v (m/s)	w (m/s) $\cdot 10^{-3}$	θ ($^{\circ}$ K)
SLSI23	180	0.05	0.170	0.134	0.58	0.087
SLSI24	360	0.05	0.180	0.168	0.92	0.088
SLSI25	600	0.05	0.220	0.256	1.62	0.098
SLSI12	1200	0.05	0.373	0.526	3.40	0.139
SLSI15	1800	0.05	0.554	0.796	5.87	0.191
SLSI18	2400	0.05	0.764	1.038	7.23	0.254
SLSI22	3600	0.07	1.204	1.270	8.56	0.377

The differences in the v and θ fields obtained at each grid point for experiments SLSI23 and SLSI15 are shown in Figs. 15-18. It can be seen that the largest differences occur close to the frontal region for the v field, but they are almost uniformly distributed at the lowest levels in the θ field for experiment SLSI15.

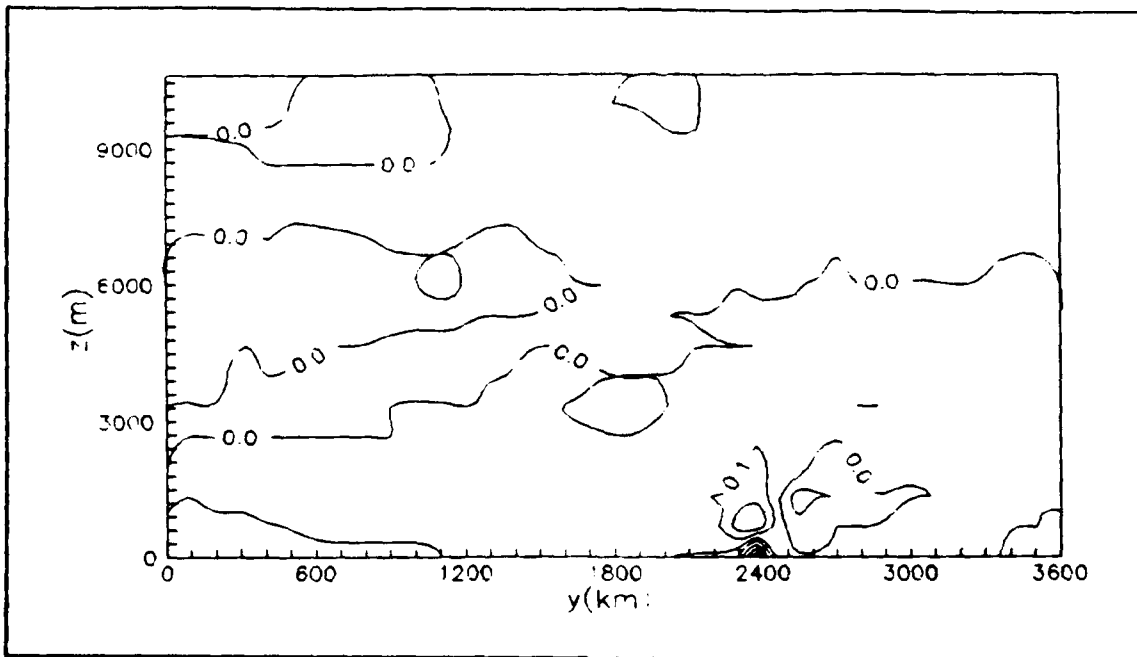


Figure 15. Differences in u component field (m/s) for experiment SLSI23 at $t = 36$ hours.

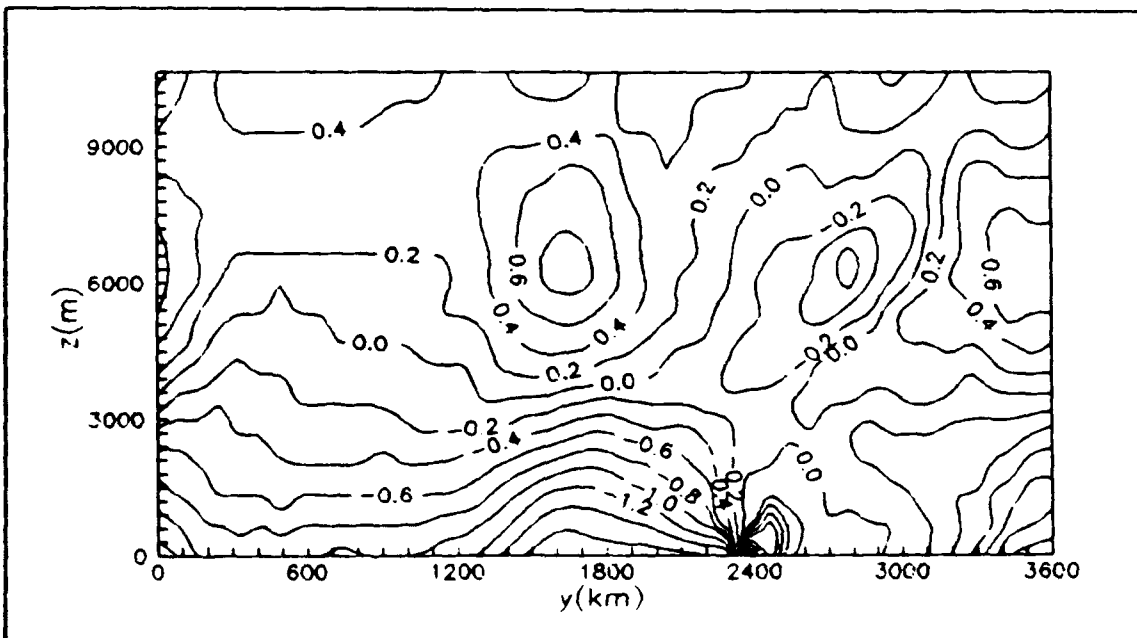


Figure 16. Differences in u component field (m/s) for experiment SLSI15 at $t = 36$ hours.

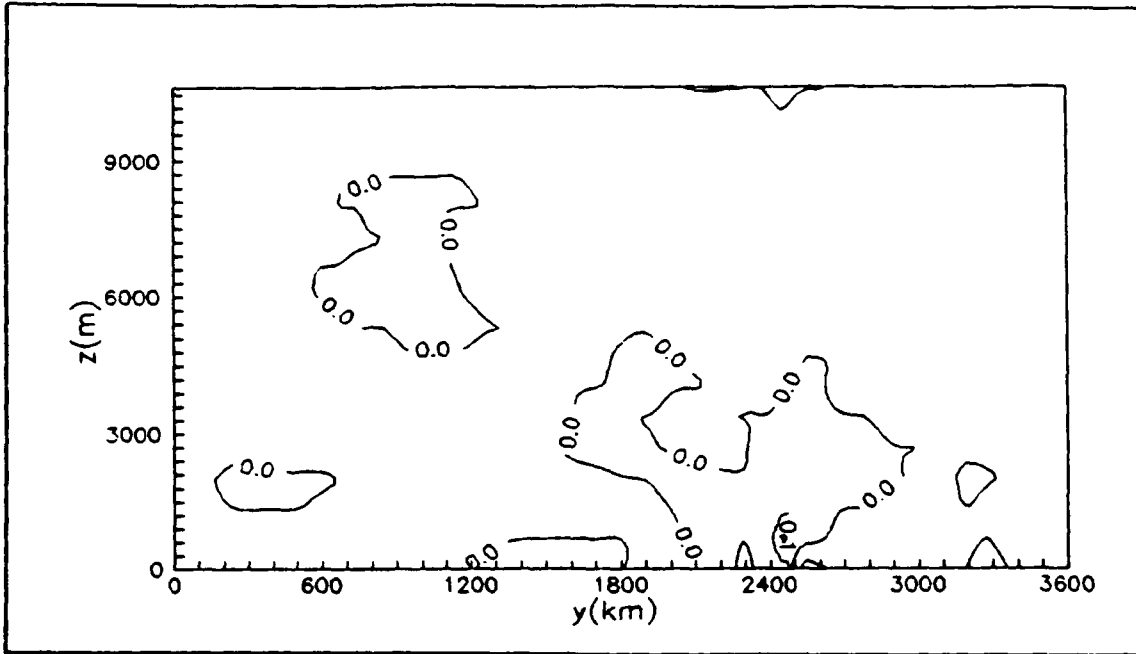


Figure 17. Differences in θ field ($^{\circ}\text{K}$) for experiment SLSI23 at $t = 36$ hours.

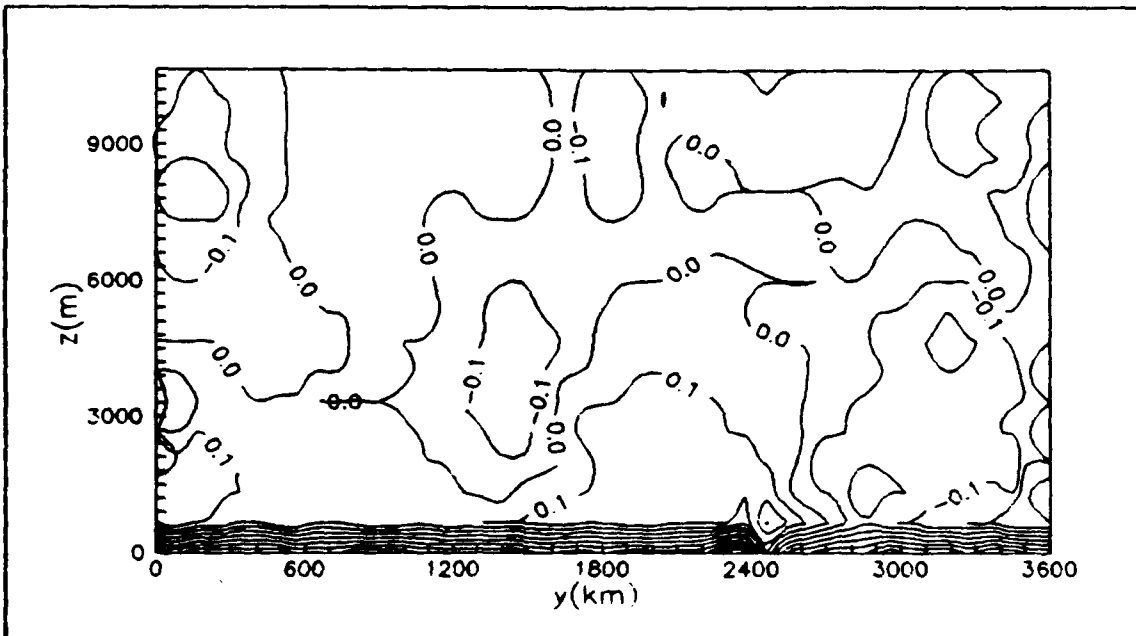


Figure 18. Differences in θ field ($^{\circ}\text{K}$) for experiment SLSI15 at $t = 36$ hours.

The second set of comparisons used as reference the same solutions obtained for experiment SLHR02 at time $t = 36$ hours. The frontal width at that time in the high resolution experiment was 99.5 km. For those SLSI experiments where the time filter controlled the high frequency oscillations, the frontal width $d = 100$ km was uniquely related to a certain time. If the solutions had no error we could suppose that for a certain d -value the velocity components and temperature fields should be the same as those obtained from the control run. Thus, the geophysical fields for the times corresponding to a d -value approximately equal to 100 km were chosen for the second set of comparisons. Table 7 gives the RMS differences obtained and the corresponding frontal widths and times used for each comparison. The values obtained show that the frontogenesis process is slower for longer time steps, since the frontal width of 100 km is reached at a later time for larger Δt . The RMS differences for u and θ are again relatively small compared to the magnitude of the values obtained in the reference solution. The differences for v and w are still relatively large with respect to the reference values, as expected. Figures 19-22 show the grid point differences of the u and θ fields for experiments SLSI23 and SLSI15.

The figures show that the largest differences occur close to the front. This characteristic of semi-Lagrangian schemes in which the large errors are confined around the scale collapse region was observed by Kuo and Williams (1990). Such a property is desirable, since the regions away from the front will not undergo a large effect of errors generated close to the region where strong gradients are present.

Figures 23-29 show the temperature distribution at the lowest computational level ($z = 167$ m) for the experiments listed in Table 5 (solid line) for comparison with the

values obtained from the control run (dashed line). It can be seen that as the time step increases the differences increase but the largest errors remain close to the frontal region.

TABLE 7. RMS DIFFERENCES FOR $d = 100$ km.

	RMS DIFFERENCES					
Experiment, $\Delta t(\text{sec.}), \gamma$	$u(\text{m/s})$	$v(\text{m/s})$	$w(\text{m/s})$ $\cdot 10^{-3}$	$\theta(^{\circ}\text{K})$	$d(\text{km})$	Time (hours)
SLSI03, 180, 0.03	0.667	0.398	2.91	0.215	101.0	38.0
SLSI06, 360, 0.03	0.683	0.422	3.01	0.240	101.4	38.2
SLSI09, 600, 0.03	0.731	0.468	3.24	0.280	100.8	38.5
SLSI12, 1200, 0.05	0.914	0.593	3.78	0.388	101.2	39.3
SLSI15, 1800, 0.05	1.031	0.622	3.92	0.452	101.5	39.5
SLSI19, 2400, 0.07	1.155	0.701	4.26	0.531	101.5	40.0
SLSI27, 3600, 0.10	1.197	0.815	5.47	0.588	103	40.0

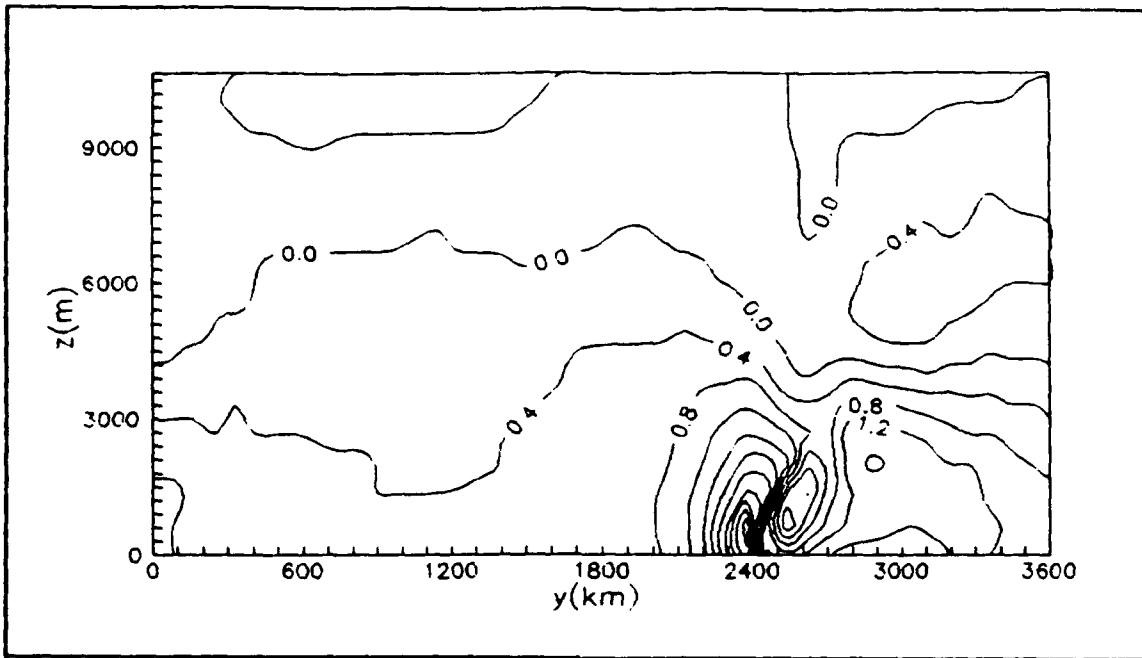


Figure 19. Differences in u component field (m/s) for experiment SLSI03 at time corresponding to $d=100$ km.

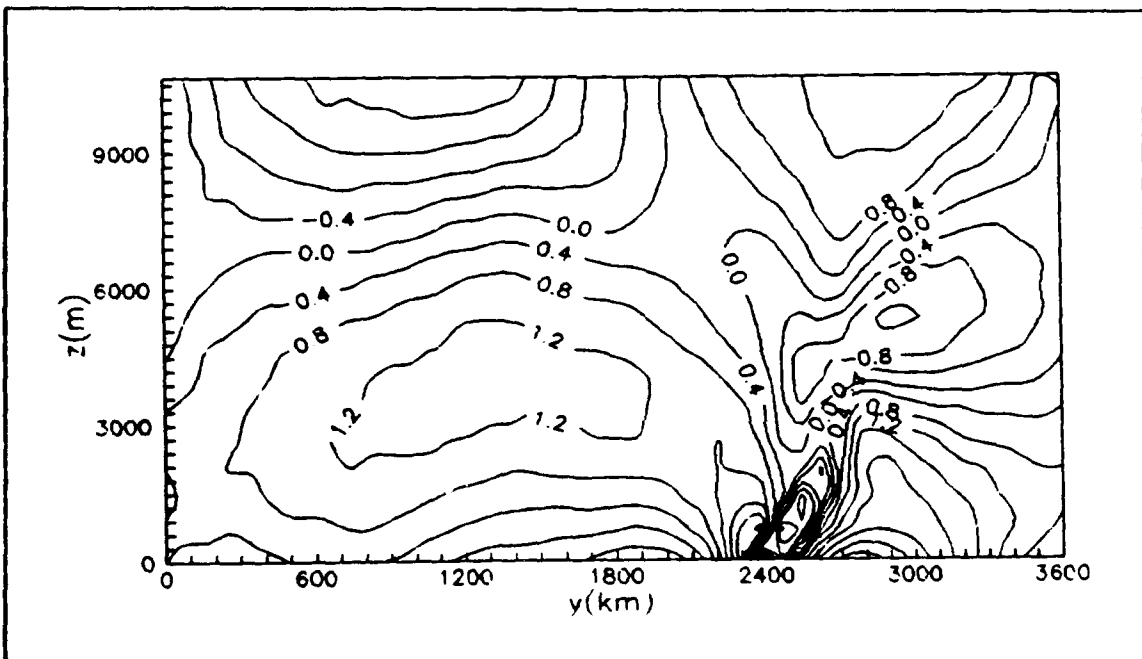


Figure 20. Differences in u component field (m/s) for experiment SLSI15 at time corresponding to $d=100$ km.

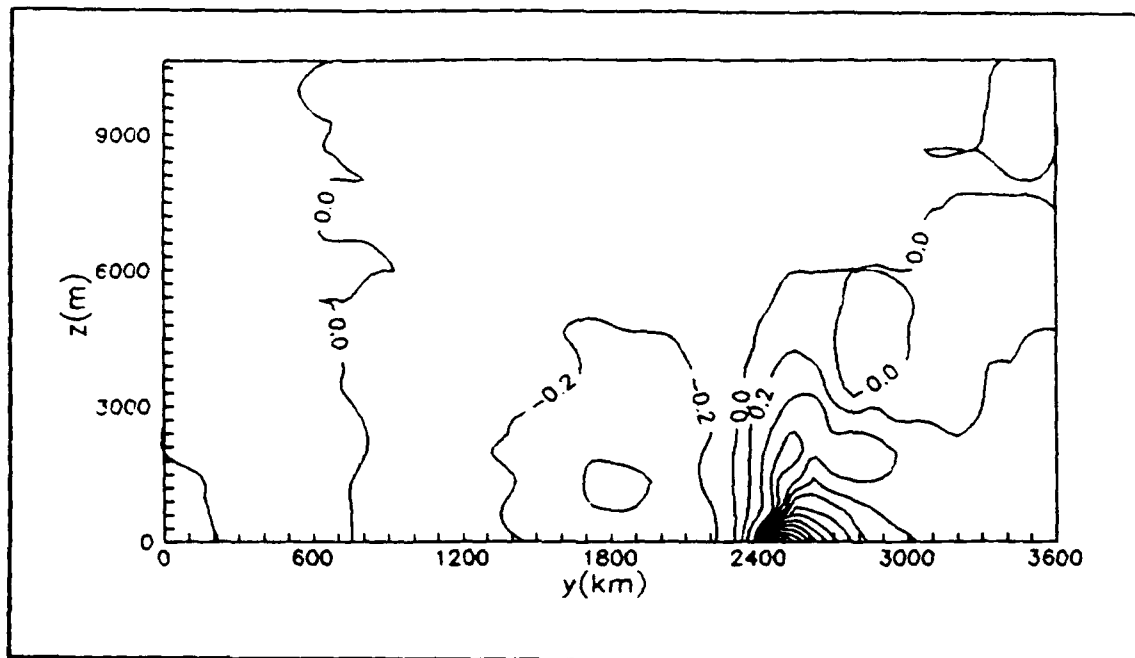


Figure 21. Differences in θ field ($^{\circ}\text{K}$) for experiment SLSI03 at time corresponding to $d=100$ km.

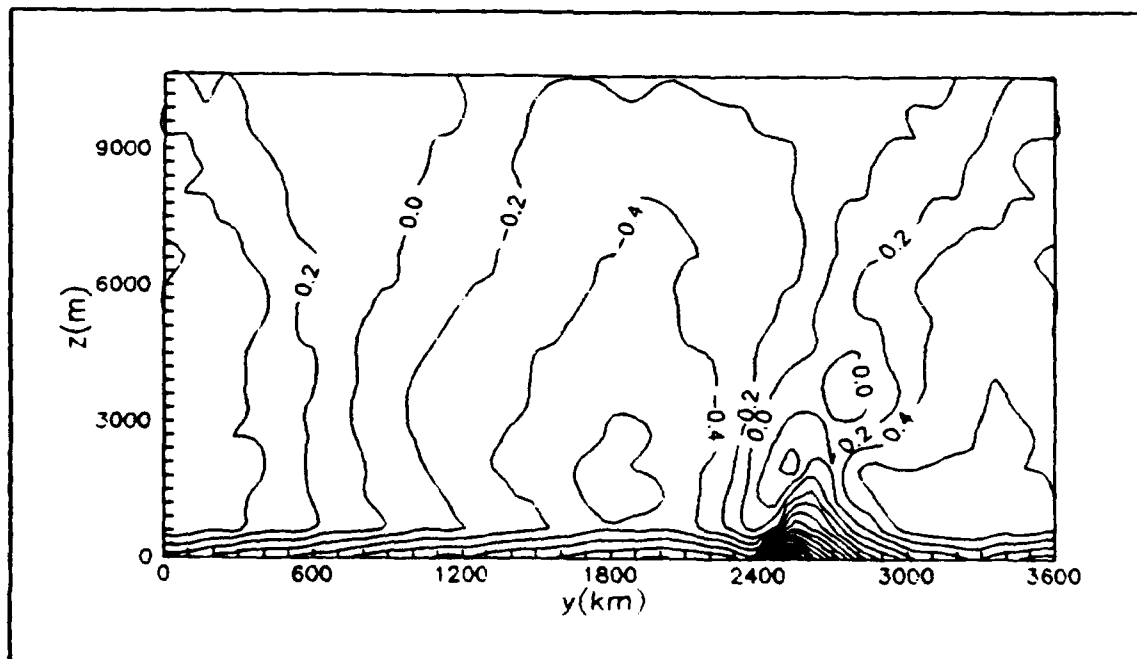


Figure 22. Differences in θ field ($^{\circ}\text{K}$) for experiment SLSI15 at time corresponding to $d=100$ km.

For this model the Courant number σ is calculated using the following expression:

$$\sigma = (|v|_{\max} + |V_d|_{\max} + |c_g|_{\max}) \frac{\Delta t}{(\Delta y/2)}, \quad (5.3)$$

where $c_{g\max}$ is the phase speed of the fastest internal gravity wave. An important result from this study is that for the SLSI experiments, σ ranged from 0.5 ($\Delta t = 180$ sec.) to 10.4 ($\Delta t = 3600$ sec.), as opposed to the CFL stability criterion that would require σ to be less than or equal to 1, and the values of the RMS differences obtained for u and θ in the experiments with large time steps remained relatively small. This result indicates that the gain in computational efficiency does not affect significantly the accuracy of the solutions obtained with the SLSI scheme.

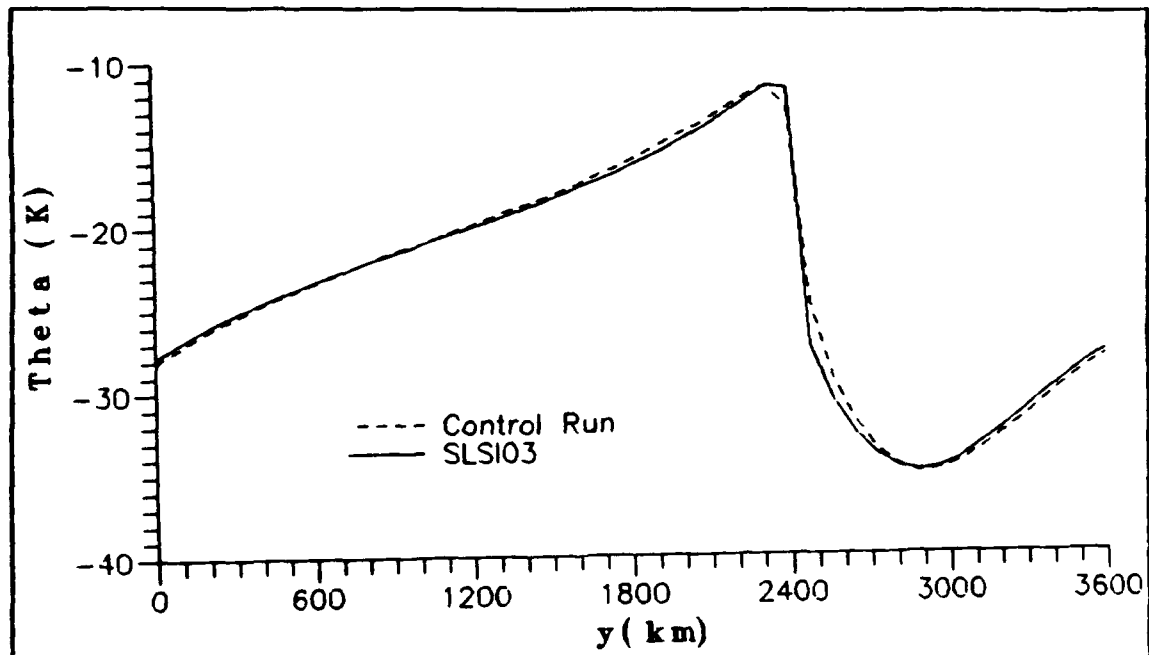


Figure 23. Temperature disturbance at $z = 167$ m, for experiment SLSI03 (solid line) and control run (dashed line), at time corresponding to $d \sim 100$ km.

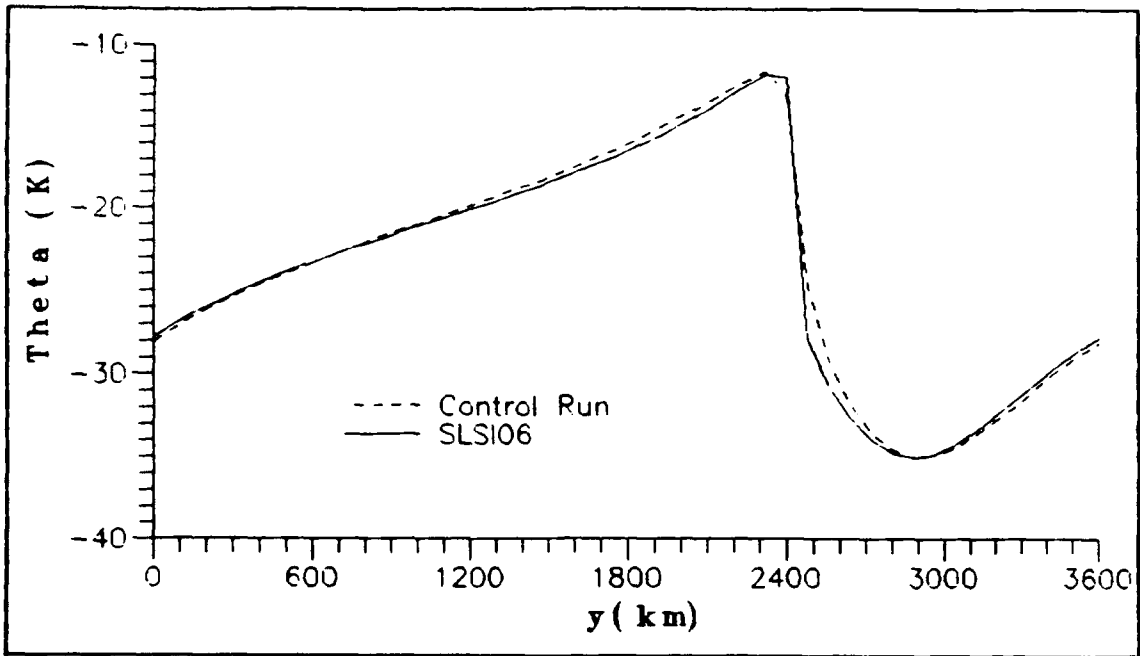


Figure 24. Same as Fig. 23 except for experiment SLSI06.

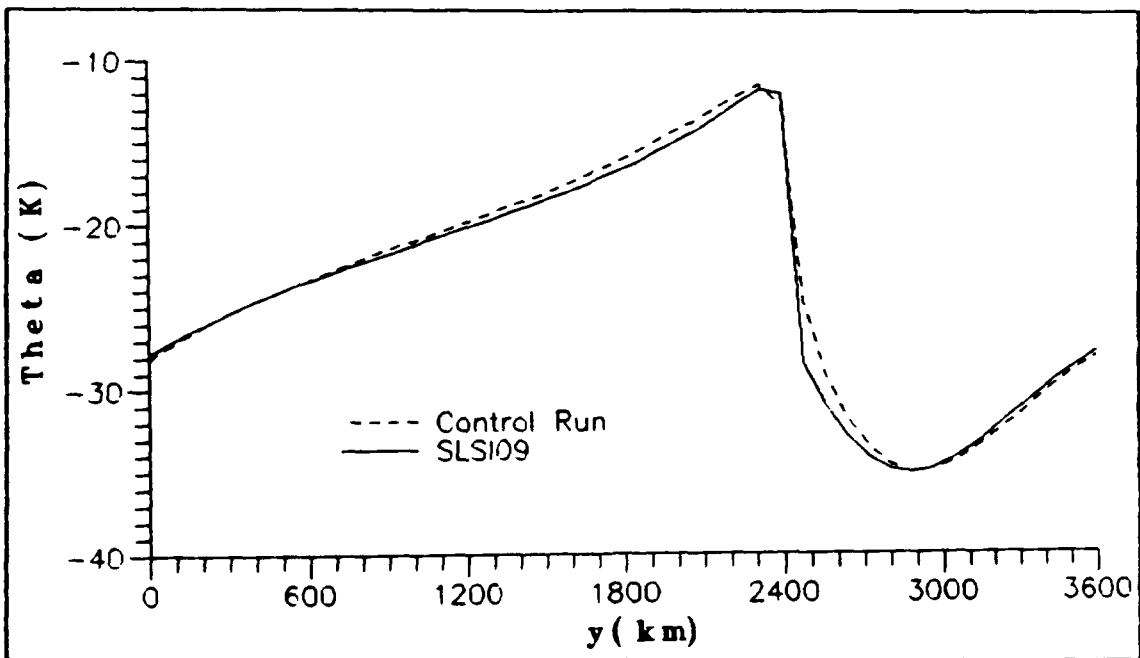


Figure 25. Same as Fig. 23 except for experiment SLSI09.

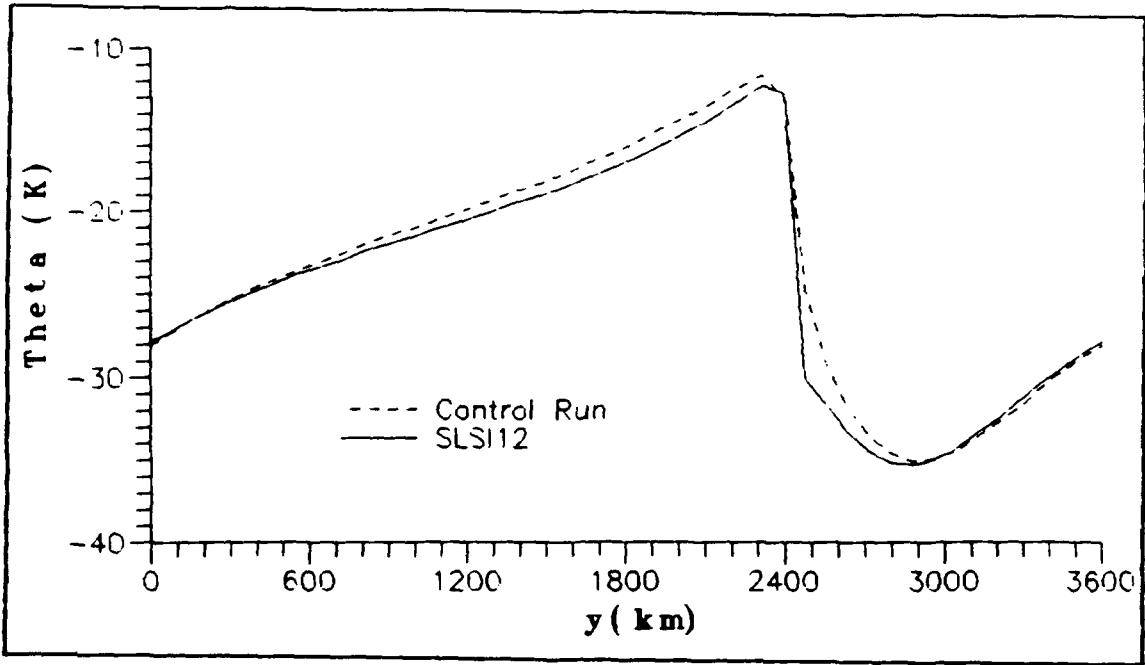


Figure 26. Same as fig. 23 except for experiment SLSI12.

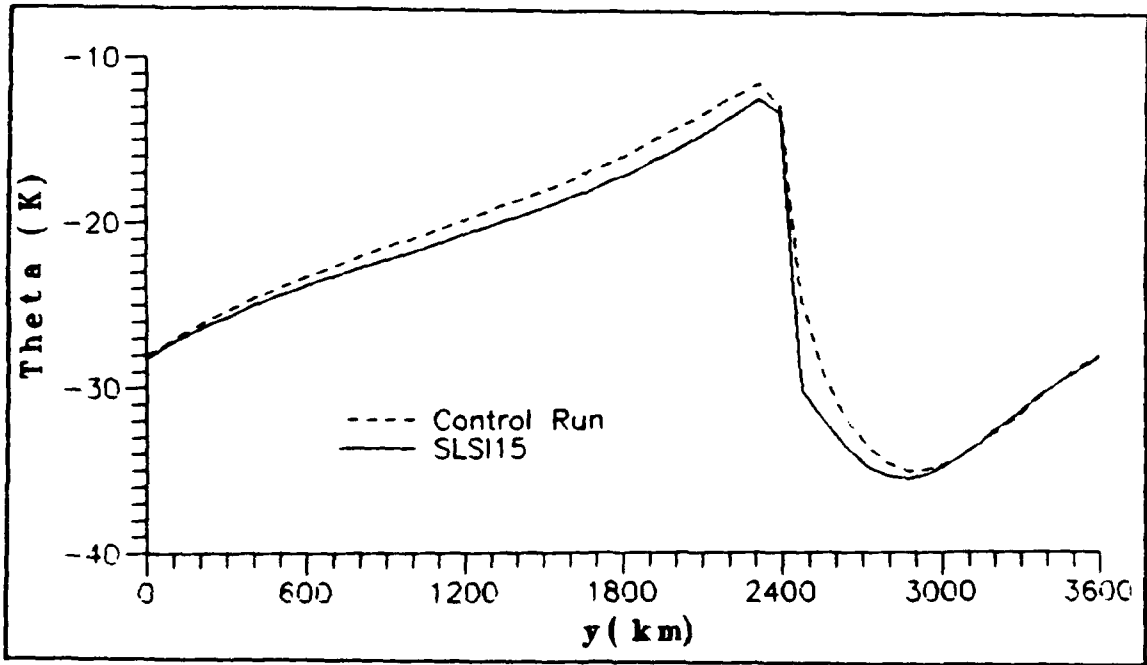


Figure 27. Same as Fig. 23 except for experiment SLSI15.

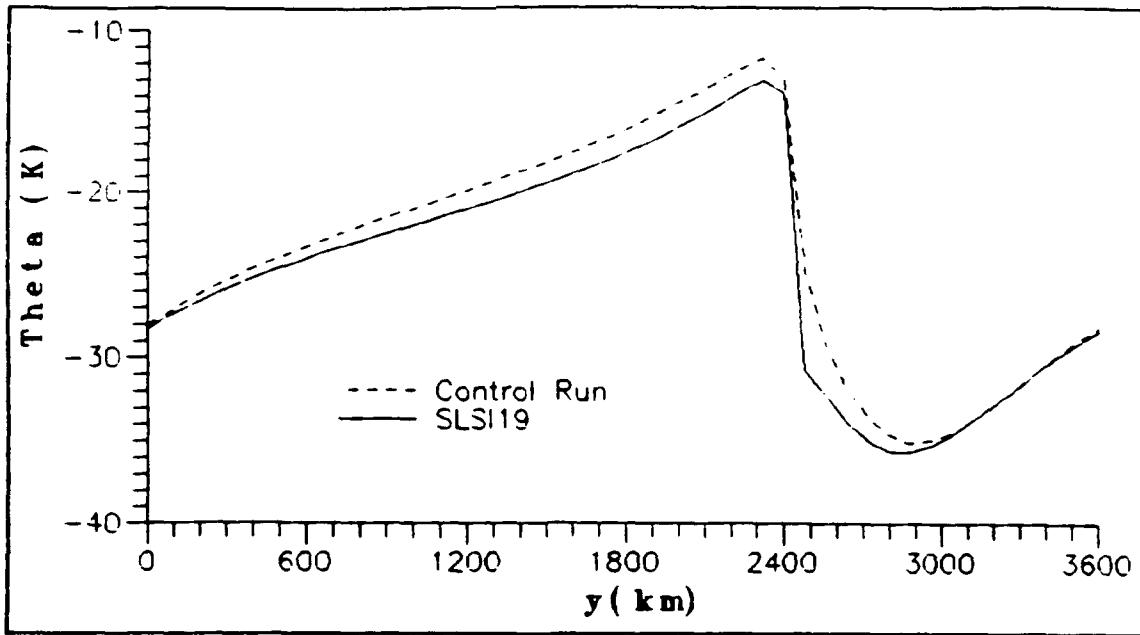


Figure 28. Same as Fig. 23 except for experiment SLSI19.

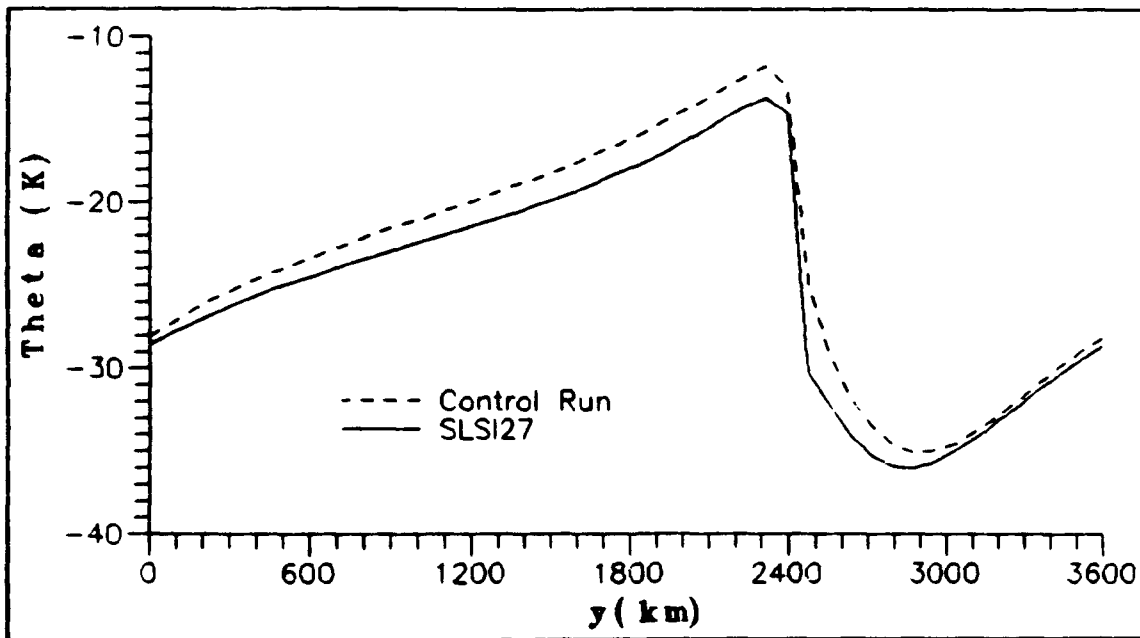


Figure 29. Same as Fig. 23 except for experiment SLSI27.

VI. SUMMARY AND CONCLUSIONS

In this study a numerical model based on the hydrostatic Boussinesq equations was used to simulate atmospheric frontogenesis driven by an irrotational non-divergent deformation wind field. The semi-Lagrangian technique was employed to integrate numerically the prognostic equations. The model assumes periodic boundary conditions in the cross-front direction and the rigid lid assumption is used as the upper boundary condition. The model also neglects along front variations. A basic sinusoidal deformation flow is introduced as the forcing of the frontogenesis process. Experiments were performed using the semi-Lagrangian technique associated with two different time schemes: explicit and semi-implicit. In the semi-Lagrangian explicit case (SLEX) bicubic splines were used to interpolate the variables in space. In the semi-Lagrangian semi-implicit case (SLSI) the variables were interpolated in the y-direction only, using one-dimensional splines. A frontal width parameter (*d-value*) was defined at the lowest computational level to describe the evolution of the frontogenetical processes. The experiments with the SLEX technique were successful in replicating the formation of a realistic front in approximately 40 hours. Different time steps were used for the integration of the model and solutions which were both numerically and physically consistent were obtained with the SLEX scheme for values of Courant numbers as large as 1.7.

The experiments with SLSI scheme presented high frequency oscillations that were eliminated by using a time filter. However, no small scale spatial oscillations were observed in the solutions. Different filtering effects were tested by changing the value

of the filtering parameter γ . The solutions obtained with the SLEX scheme were not affected by the time filter, whereas the SLSI solutions showed that stronger filtering was necessary for larger time steps.

The SLSI scheme showed to be more successful in handling the scale collapse process than the SLEX scheme, since the fronts reproduced by the former had minimum widths smaller than those obtained by the latter. The SLSI scheme presented a tendency of slowing down the frontogenesis process for increasing time steps.

Experiments were performed with the SLSI scheme with time steps as long as 3600 seconds, corresponding to a Courant number greater than 10. The solutions obtained were perfectly stable, and the accuracy was not significantly degraded, even for longer time steps.

The SLSI solutions also had the characteristic of constraining the largest errors close to the scale collapse region. Such a characteristic is desirable since the errors will have a smaller impact on the solutions in regions away from the front.

The results obtained in this study suggest that the SLSI technique is appropriate for mesoscale regional models since it is computationally efficient and produces accurate results. A different formulation of the scheme where two-dimensional interpolation of variables were allowed should be studied to verify if there would be a significant positive impact on the accuracy of the solutions. Also, effects of surface topography and physical processes like advection of the frontal system, friction, vertical shear of the basic wind field and moisture should be investigated in future studies.

LIST OF REFERENCES

- Asselin, R. A., 1972: Frequency filter for time integrations. *Mon. Wea. Rev.*, **100**, 487-490.
- Arakawa, A., and V. R. Lamb, 1977: Computational design of the basic dynamical processes of the UCLA general circulation model, *Methods in Computational Physics, Vol. 17*. Academic Press, 174-265, 337 pp.
- de Boor, C., 1962: Bicubic spline interpolation. *J. Math. Phys.*, **41**, 212-218.
- Haltiner, G. J., and R. T. Williams, 1980: Numerical Prediction and Dynamic Meteorology, 2d. ed. Wiley and Sons, 477 pp.
- Kuo, H. C., and R. T. Williams, 1990: Semi-Lagrangian solutions to the inviscid Burgers equation. *Mon. Wea. Rev.*, **118**, 1278-1288.
- Marchuk, G. I., 1982: Methods of Numerical Mathematics, 2d. ed. Springer-Verlag, 510 pp.
- Monk, K.B., 1989: Semi-Lagrangian, semi-implicit solutions of the shallow water equations in one dimension. M. S. thesis, Naval Postgraduate School, Monterey, CA, 41 pp.
- Pielke, R. A., 1984: Mesoscale Meteorological Modeling. Academic Press, 612 pp.
- Pudykiewicz, J. and A. Staniforth, 1984: Some properties and comparative performance of the semi-Lagrangian method of Robert in the solution of the advection-diffusion equation. *Atmos-Ocean*, **22**, 283-308.
- Robert, A., J. Henderson and C. Turnbull, 1972: An implicit time integration scheme for baroclinic models of the atmosphere. *Mon. Wea. Rev.*, **100**, 329-335.

- , 1981: A stable numerical integration scheme for the primitive meteorological equations. *Atmos-Ocean*, 19, 35-46.
- , T. L. Yee and H. Ritchie, 1985: A semi-Lagrangian and semi-implicit numerical integration scheme for multi level atmospheric models. *Mon. Wea. Rev.*, 113, 388-394.
- Sawyer, J. S., 1963: A semi-Lagrangian method of solving the vorticity advection equation. *Tellus*, 15, 336-342.
- Stone, P. H., 1966: Frontogenesis by horizontal wind deformation fields. *J. Atmos. Sci.*, 23, 455-565.
- Williams, R. T., 1972: Quasi-geostrophic versus non-geostrophic frontogenesis. *J. Atmos. Sci.*, 29, 3-10.
- , M. S. Peng and D. A. Zankofski, 1991: Effects of topography on fronts. Submitted to *J. Atmos. Sci.*

INITIAL DISTRIBUTION LIST

	No. Copies
1. Defense Technical Information Center Cameron Station Alexandria, VA 22304	2
2. Library, Code 52 Naval Postgraduate School Monterey, CA 93943-5000	2
3. Chairman (Code OC/Co) Department of Oceanography Naval Postgraduate School Monterey, CA 93943-5000	1
4. Chairman (Code MR/Hy) Department of Meteorology Naval Postgraduate School Monterey, CA 93943-5000	1
5. Professor Roger T. Williams (Code MR/Wu) Department of Meteorology Naval Postgraduate School Monterey, CA 93943-5000	5
6. Professor Melinda S. Peng (Code MR/Pg) Department of Meteorology Naval Postgraduate School Monterey, CA 93943-5000	1

7 Lieutenant Commander Ricardo Carvalho de Almeida 3
Diretoria de Hidrografia e Navegação
R. Barão de Jaceguay s.n
Ponta da Armação, Niterói
RJ, BRAZIL 24040